

THOMAS P. OGDEN

REORIENTATION
DYNAMICS OF
NITRATE IN WATER

DEPARTMENT OF PHYSICS, STOCKHOLM UNIVERSITY

SCIENCE TEACHES US TO ACCEPT REALITY WITH WONDER AND
ADMIRATION, NOT TO MENTION THE DEEP JOY AND AWE THAT THE
NATURAL ORDER OF THINGS BRINGS.

— LISE MEITNER



Stockholm
University

Copyright © 2011 Thomas P. Ogden

PUBLISHED BY DEPARTMENT OF PHYSICS, STOCKHOLM UNIVERSITY

Printed in Stockholm, Sweden. August 2011

Contents

<i>1</i>	<i>Introduction</i>	<i>9</i>
<i>2</i>	<i>Theoretical Background</i>	<i>15</i>
<i>3</i>	<i>Computational Methods</i>	<i>25</i>
<i>4</i>	<i>Results & Discussion</i>	<i>29</i>
<i>5</i>	<i>Conclusions</i>	<i>53</i>
<i>A</i>	<i>The Cutout Tool</i>	<i>55</i>
	<i>Bibliography</i>	<i>59</i>

Abstract

The nitrate anion in solution functions as a probe of its environment through the spectroscopy of its vibrational modes. In water, dynamic hydrogen-bonding with the hydration shell is manifested in the symmetry breaking of nitrate's asymmetric stretches.

THIS COMPUTATIONAL STUDY aims to support recent experimental evidence of frequency dependence in the reorientation of nitrate in water and provide a direct molecular picture of the mechanisms involved. I run molecular dynamics simulations of a potassium nitrate pair in water to analyse structural properties and dynamic behaviour of the system. I make quantum chemistry calculations on small complexes of nitrate with up to two water molecules and on full hydration shell structures cut out from the molecular dynamics trajectories.

I find that the reorientation is driven by two mechanisms: an ultrafast (sub-picosecond) libration and a fast (picosecond) rotation. Based on direct observation of the simulated trajectories and recent theoretical study, the picosecond rotation is attributed to a sudden jump mechanism. In both motions, reorientation is faster with higher temperature. No anisotropy is found within time correlation functions of the molecular vector reorientation nor of the angular velocity.

The asymmetric stretch symmetry breaking in hydration shells is consistent: the lowest vibrational frequency corresponds to the longest internal nitrogen-oxygen bond and hence to that oxygen being the most strongly hydrogen-bonded. This direct picture of the fluctuating split in the asymmetric stretch modes offers an explanation as to why the frequency dependence is not observed as an anisotropy in molecular vector reorientation, and suggests a next move toward detecting it in an extension to this work.

1

Introduction

The nitrate anion, NO_3^- , is a naturally-occurring species crucial to understanding the chemistry of Earth's soils, skies and seas.

Nitrification by bacteria in soil — the oxidation of ammonia into nitrites (NO_2^-) and then nitrates — is a key process in the nitrogen cycle, providing this essential element in a form that can be used by plant life.

Nitrate salts are highly hygroscopic, seeding cloud formation¹ and nitric acid, HNO_3 , contributes significantly to acidification in the troposphere.² The abundance of nitrate ions in ice cores facilitates study of the climate and atmospheric chemistry of the planet's history.³

High nitrate levels in rivers and oceans can cause eutrophication and the death of marine life,⁴ and must be monitored and controlled in drinking water as in extreme cases may pose a threat to humans.

Nitrate is used industrially in inorganic fertilisers, in the production of explosives and in glassmaking. These human influences can dramatically affect nitrate levels in ecosystems.⁵

STUDY OF THE NITRATE SPECIES in solution chemistry is useful in its own right. Nitrate can provide information about its environment via the spectroscopy of its vibrational modes.⁶ Conversely, solvent effects on the dynamics of nitrate and other ions is key to chemical reaction mechanisms and solute transport.⁷

1.1 Symmetry Breaking in Asymmetric Stretch Modes

Many small molecules belong to highly-symmetric point groups in their isolated state, which makes certain vibrational normal modes degenerate. In solution, interactions between solute and solvent may modify the charge distribution and geometry of the solute molecule. Symmetry is broken.

The isolated nitrate ion is planar with D_{3h} symmetry. The negative charge on the ion is spread equally among the three identical oxygen atoms, each forming partial double bonds with the central nitrogen.

As a nonlinear molecule with $N = 4$ atoms, the nitrate ion has

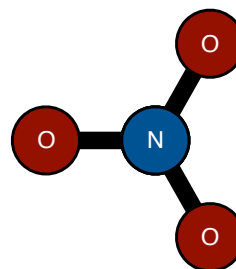


Figure 1.1: The nitrate ion. One nitrogen atom surrounded by three oxygen atoms in a trigonal planar arrangement.

¹ Ramesh et al., 2009.

² Guimbaud et al., 2002.

³ Abbatt, 1997.

⁴ Smith et al., 1999.

⁵ World Health Organisation, 2008.

⁶ Ramesh et al., 2009.

⁷ Laage and Hynes, 2007.

$3N - 6 = 6$ vibrational modes. These are the N-O symmetric stretch ν_1 , the out-of-plane bend ν_2 , the two N-O asymmetric stretches ν_{3x} and ν_{3y} , and the two O-N-O in-plane bends ν_{4x} and ν_{4y} . The numbering is per spectroscopic convention and the x, y tags indicate the axis along which the nitrogen atom moves, as shown in figures 1.2 and 1.3 for the asymmetric stretch.

The asymmetric stretch modes are degenerate in the isolated state, with $\nu_3 \approx 1370 \text{ cm}^{-1}$. However, in a polar solution the environment lifts the degeneracy of these stretches and we see a double peak in both infrared (IR) and Raman spectra.

In a protic solvent like water, symmetry is broken by transient hydrogen bonding (H-bonding) between water molecules and one or more of the oxygen atoms in nitrate. The H-bond results in a charge-redistribution in the nitrate ion and the molecule's internal bonds is weakened, changing the effective symmetry to C_{2v} (one unique N-O bond length) or C_s (three different N-O bond lengths).

This symmetry breaking has been observed in resonance Raman spectroscopy of nitrate in H-bonding solvents by Waterland & Kelley.⁸ An average splitting of $\Delta\nu_3 \approx 60 \text{ cm}^{-1}$ is seen in dilute aqueous solution.

SEVERAL THEORETICAL STUDIES have looked at the symmetry breaking in nitrate.

Waterland et al.⁹ found ground state structures and vibrational frequencies for small complexes — nitrate with one and two water molecules — with the *ab initio* Hartree-Fock (HF) method.¹⁰ By comparing split results with the nitrate ion in salts having known crystal structures, they concluded that an average split of $\sim 60 \text{ cm}^{-1}$ suggests the most probable solution structure has C_s symmetry. They found that the bulk structure is more asymmetric on average than the optimised small complexes.

Lebrero et al.¹¹ made a hybrid quantum-classical (QM/MM) computational study looking at nitrate in aqueous clusters, coupling a density functional Hamiltonian to a classical bath. Using a molecular dynamics (MD) simulation of nitrate with 124 water molecules, they found the RMS of N-O bond distance separation to be $\sim 0.02 \text{ \AA}$. They found that residence times of asymmetric configurations are in the picosecond range, and are determined primarily by solvent dynamics of the first hydration shell.

Ramesh et al.¹² used a perturbative solute-solvent coupling approach in a theoretical study. They constructed a reference Hamiltonian H_0 , first with two modes (only ν_{3x} and ν_{3y}) then with six (the ground state, ν_{3x} , ν_{3y} and their first three overtones). They extracted instantaneous solvent forces and force gradients $\delta V(t)$ from MD simulations, and so developed a time-dependent Hamiltonian $H(t) = H_0 + \delta V(t)$ to solve.

They found a mean splitting $\Delta\nu_3 = 24.1 \text{ cm}^{-1}$ in the two-mode and 21.7 cm^{-1} in the six-mode study, both understating the observed result. They note an absence of a noticeable dependence on

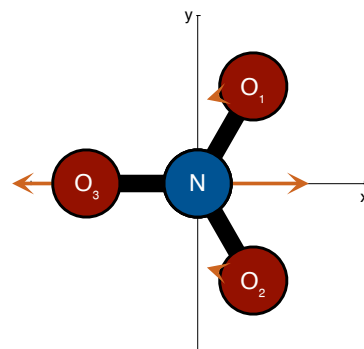


Figure 1.2: Asymmetric stretch mode ν_{3x} .

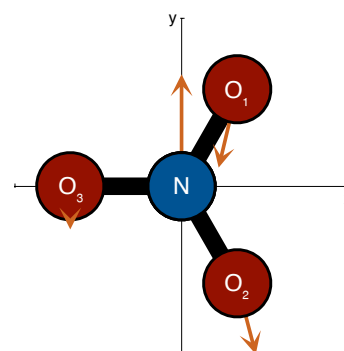


Figure 1.3: Asymmetric stretch mode ν_{3y} .

⁸ Waterland and Kelley, 2000.

⁹ Waterland et al., 2001.

¹⁰ See section 2.2 for a brief discussion of quantum chemistry methods, including HF.

¹¹ Lebrero et al., 2002.

¹² Ramesh et al., 2009.

the in-plane orientation of the N-O asymmetric stretch force.

1.2 Rotational Dynamics

The motion of the nitrate anion in aqueous solution has long attracted experimental interest, and has been subject to IR, Raman and NMR techniques.¹³

Whittle and Clarke used a depolarised Rayleigh light scattering technique to study nitrate reorientation and discuss a coupled rotation between the water and nitrate, which they describe as a ‘cogwheel effect’.¹⁴

Nakahara and Emi, using NMR, found that the correlation time for the in-plane orientation of the nitrate anion depends linearly on concentration.¹⁵

The commonly-held view on the reorientation of water molecules has been of *rotational diffusion*, where molecules change orientation in small angular steps. This picture was described by Debye in the 1920s.¹⁶

The arrival of femtosecond IR spectroscopy has given us a sharp new tool to examine hydrogen bond dynamics in water and ionic hydration shells more closely.¹⁷ This, alongside other experimental and theoretical work, suggests a different mechanism whereby the molecules rotate in sudden, large jumps.^{18,19}

The IR studies have focused on water dynamics rather than anion reorientation. The IR technique for investigating reorientation dynamics is limited by the lifetime of the vibration, which tends to be short in aqueous solution.

FEW THEORETICAL STUDIES have directly investigated rotational dynamics of nitrate in water.

Laaksonen and Kovacs studied the rotation of nitrate in water using NMR relaxation and with MD simulation. They compared in-plane and end-over-end reorientation, and found that the end-over-end motion was slower, with a correlation time $\tau = 2.72$ ps, than the in-plane, at $\tau = 1.85$ ps.²⁰

Laage and Hynes investigate rotational dynamics in the first hydration shell of a different anion, chloride, through molecular simulation.²¹ They find a labile hydration sphere structure, and account for dynamic behaviour with an extended jump model.

1.3 Motivation from Experiment

My motivation for this computational study is the recent and ongoing experimental work on the reorientation dynamics of nitrate in water by Thøgersen et al. at the University of Aarhus, Denmark.

The Aarhus group used femtosecond IR spectroscopy directly following the UV charge transfer-to-solvent (CTTS) transition to measure reorientation times of nitrate ions in water as a function of temperature and of probe frequency.

¹³ Laaksonen and Kovacs, 1994.

¹⁴ Whittle and Clarke, 1983.

¹⁵ Nakahara and Emi, 1999.

¹⁶ Debye, 1929.

¹⁷ Laage and Hynes, 2007.

¹⁸ Laage et al., 2011.

¹⁹ See section 2.1.5 for a description of *jump models*.

²⁰ Laaksonen and Kovacs, 1994.

²¹ Laage and Hynes, 2007.

The CTTS transition is an electronic excitation to a quasi-bound state supported by the hydration sphere, arising from the π to π^* molecular transition.²²

A linearly-polarised femtosecond ultraviolet (UV) pump pulse at 200 nm, excites this π to π^* transition efficiently in nitrate, preferably exciting nitrate molecules whose plane aligns parallel to the direction of polarisation. The lifetime of the excited state is long enough to exclude the excited nitrate ions from the IR survey of the asymmetric stretch. The orientation distribution of the remaining *unexcited* nitrate ions becomes anisotropic.

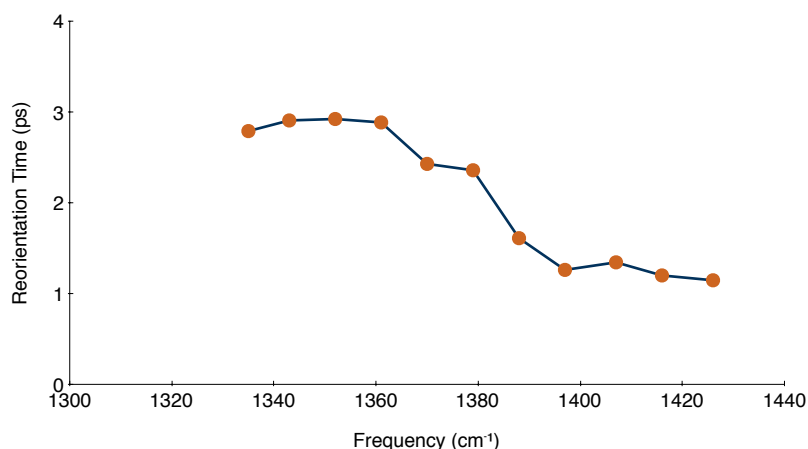
This transient anisotropy is then measured using an IR probe, close to the prominent in-plane asymmetric stretch frequencies²³ seen at $\sim 1370\text{ cm}^{-1}$. As unexcited nitrate ions reorient back into the plane parallel to the pump pulse, more molecules become available to absorb a time-delayed IR probe polarised either parallel or perpendicular to the pump pulse. In this way Thøgersen et al. determine reorientation dynamics of the nitrate molecule in thermal equilibrium and, as the CTTS transition is localised on the nitrate ion, they measure local molecular reorientation rather than a distributed effect.

The decay in polarisation anisotropy $r(t)$ is modelled in the standard exponential form²⁴

$$r(t) = r_0 \exp\left(\frac{-t}{\tau}\right) \quad (1.1)$$

Looking at a 0.01 M solution of KNO_3 in water at 300 K and 1 atm, they find a reorientation time τ of ~ 2.0 ps.

Thøgersen et al. also observe that, remarkably, the reorientation time depends on the probe frequency.²⁵ Moreover, the reorientation time appears to be correlated with the two symmetry-broken asymmetric stretch frequencies. At the lower asymmetric stretch frequency $\nu_{3\text{lo}}$, the reorientation time is around 2.7 ps and at the higher asymmetric stretch $\nu_{3\text{hi}}$, it is around 1.3 ps (see figure 1.4).



²² Thøgersen et al., 2008.

²³ See section 1.1 for a discussion of the asymmetric stretch modes of nitrate.

²⁴ Thøgersen et al., 2008.

²⁵ Thøgersen, 2011.

Figure 1.4: Experimental results showing the frequency dependence of the anion anisotropy decay in a 0.01 M solution of KNO_3 in water at 300 K and 1 atm.

These results from an innovative technique in femtosecond spec-

troscopy offer an intriguing view on the dynamic behaviour of the nitrate anion in aqueous solution. The results motivate a computational study to characterise the structural and dynamic properties of nitrate in water, and to determine the solvent forces which underly its behaviour.

Strong H-bonds between water and oxygen in nitrate are believed to be an important factor. The frequency-dependence of the anisotropy suggests that the H-bonds interacting with the nitrate in solution are maintained through the rotation, over a few picoseconds. By MD simulation and quantum chemistry modelling of clusters, we hope to resolve in detail the mechanisms involved.

1.3.1 Photolysis

The Aarhus group have also used femtosecond absorption spectroscopy to determine the formation and relaxation of the primary products of nitrate photolysis.²⁶

They found that 44% of the excited NO_3^- molecules return to the vibrationally hot electronic ground state in 2 ps. Concurrently, 48% of the excited NO_3^- molecules isomerise to ONOO^- , while the remaining molecules dissociate to $[\text{NO} + \text{O}_2]^-$, as shown in figure 1.5.

²⁶ Madsen et al., 2003.

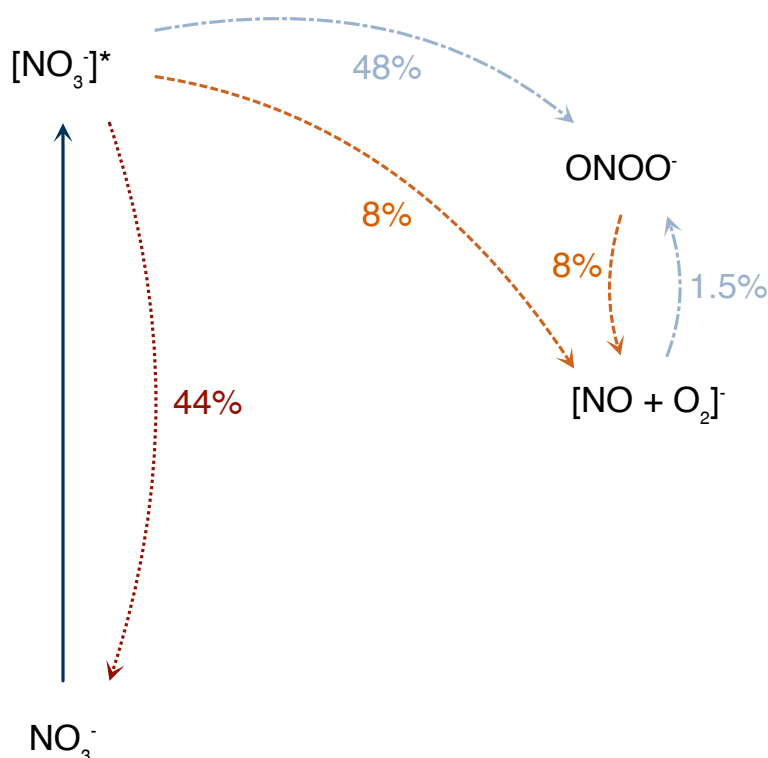


Figure 1.5: The photodynamics of NO_3^- (aq) when excited at 200 nm. Madsen et al., 2003.

The contribution to absorption spectra from this relaxation pathway complicates analysis of the data, but as it only overlaps partially with the vibrational signature of nitrate ions left unexcited by

the UV pulse, this does not pose a severe problem.

1.4 *Aims of This Study*

My central concern in this computational study will be to simulate the dynamic behaviour of nitrate in water, with the aim of supporting the experimental reorientation results by Thøgersen et al. and of describing the molecular mechanisms behind this behaviour. I'll look for any dependence on the temperature of the solution.

The great potential of simulation is the possibility of a direct molecular picture to explain experimental results.

I'll investigate the link between reorientation and vibrational frequency by modelling the nitrate anion in water to determine its vibrational and electronic excitations, and how these are affected by the geometry of the solvent.

The computational methods I will use are discussed in chapter 3. First, a summary of the theoretical background to these methods.

2

Theoretical Background

The study of solvent dynamics necessitates approximate potential models and classical dynamics, and we can gain a detailed molecular understanding of solvent structure and dynamics using MD simulation. The *pump-probe* spectroscopy experiments described in section 1.3 measure reorientation in the form of decaying anisotropy, which can be matched to trajectory analysis of MD simulations in the form of time correlation functions.

Calculations of the vibrational spectrum of molecules and their electronic excitations require a quantum mechanical approach because of the fundamental dependence of these on molecular orbitals. For this we require the methods of quantum chemistry.

2.1 *Molecular Dynamics*

The huge number of states accessible to a many-particle system cannot possibly be visited in entirety by any computer we might use to determine its physical properties.¹ We must choose a relatively small, but representative, subset of states to sample properties of the system we define.

¹ Thijssen, 2007, p197.

Nuclei are heavy enough that we may model them as classical particles in a potential field, subject to Newton's laws. In classical *molecular dynamics* (MD) simulation we integrate the Newtonian equations of motion for each particle numerically using a finite difference method. A range of methods exist for particular priorities. For any method, appropriate boundary conditions are important for a successful simulation.

A key advantage of MD sampling is that it offers dynamic information about the system, essential for an investigation of reorientation behaviour.

2.1.1 *Finite Difference Methods*

The simple idea of MD is to take the molecular positions and velocities at a time t and, by solving the differential equations describing their motion, to obtain these positions and velocities at a later time $t + \delta t$ to a sufficient accuracy.² These equations are solved numerically, step-by-step.

² Allen and Tildesley, 1989, p73.

The choice of numerical method for a particular case depends on the relative importance of key factors. Computationally, we would like the simulation to be fast, to require little memory and to permit a long time step δt . Physically, we would like to keep as close as possible to the true classical trajectory. We must also satisfy the conservation laws for energy and momentum.

Any two approximate trajectories starting close will diverge quickly in a numerical integration, so following a true classical trajectory is difficult. Fortunately, this is not so important in our MD system. Our aim is to sample the states available to the ensemble, so it is more important that we conserve energy and momentum. We will generate good ensemble averages by staying close to the constant energy hypersurface in phase space.³ A good algorithm permits a large time step while preserving reasonable energy conservation.

³ Allen and Tildesley, 1989, p76.

THE VERLET ALGORITHM is a widely-used, simple and reliable integration method.⁴ The step for a molecule of unit mass at time t with position $\mathbf{r}(t)$ subject to a force $\mathbf{F}(t)$ is given by

⁴ Thijssen, 2007, p201.

$$\mathbf{r}(t + \delta t) = 2\mathbf{r}(t) - \mathbf{r}(t - \delta t) + \delta t^2 \mathbf{F}(t) \quad (2.1)$$

The error for each time step is of order $\mathcal{O}(\delta t^4)$. However, the algorithm requires *two* positions to start, $t = 0$ and $t = \delta t$. If we only have the initial position, we must calculate the latter with a lower-order approximation.

The velocities $\mathbf{v}(t)$ are not explicitly required for the Verlet integration step, but we can calculate them during the simulation as

$$\mathbf{v}(t) = \frac{\mathbf{r}(t + \delta t) - \mathbf{r}(t - \delta t)}{2\delta t} + \mathcal{O}(\delta t^2). \quad (2.2)$$

TWO POPULAR VARIATIONS on the Verlet method are the *velocity Verlet* and *leap-frog* algorithms.

Using the same notation as above, the velocity Verlet integration steps for r and v are

$$\mathbf{r}(t + \delta t) = \mathbf{r}(t) + \delta t \mathbf{v}(t) + \delta t^2 \mathbf{F}(t) \quad (2.3)$$

$$\mathbf{v}(t + \delta t) = \mathbf{v}(t) + \delta t (\mathbf{F}(t + \delta t) + \mathbf{F}(t)). \quad (2.4)$$

In the leap frog integration, the position and velocity updates are out of phase by half a time step, evaluated strictly in order as

$$\mathbf{v}(t + \delta t/2) = \mathbf{v}(t - \frac{1}{2}\delta t) + \delta t \mathbf{F}(t) \quad (2.5)$$

$$\mathbf{r}(t + \delta t) = \mathbf{r}(t) + \delta t (\mathbf{v}(t + \frac{1}{2}\delta t)). \quad (2.6)$$

Both these methods have the same theoretical order of error as the original Verlet, $\mathcal{O}(\delta t^4)$, but are more stable with respect to numerical error due to finite precision arithmetic.

A benefit of these Verlet-type algorithms is that they are time-reversible, which can improve energy conservation over long simulations.⁵ The fact that velocities appear directly also facilitates coupling to an external heat bath.

⁵ Jensen, 2006, §14.2.1.

2.1.2 Force Fields

The forces acting on each atom in an MD simulation are defined by the gradient of potential energy, as functions of the distances between atoms.⁶ Accurate intramolecular and intermolecular potential terms are required to define a force field

⁶ Lyubartsev and Laaksonen, 2000

$$U = U_{\text{inter}} + U_{\text{intra}}. \quad (2.7)$$

These are usually specified in a parameterised form either by *ab initio* calculations, by fitting the results of simulations to empirical data or by some semi-empirical hybrid of the two. The widely-used assumption that the atoms only interact pairwise is a good one and immediately reduces computational expense, requiring calculations no higher than $\mathcal{O}(N^2)$.

A typical intermolecular force field U_{inter} is

$$U_{\text{inter}} = \sum_{i \neq j} \left(4\varepsilon_{ij} \left[\left(\frac{\sigma_{ij}}{r_{ij}} \right)^{12} - \left(\frac{\sigma_{ij}}{r_{ij}} \right)^6 \right] + \frac{q_i q_j}{r_{ij}} \right) \quad (2.8)$$

for two atoms separated by a distance r with Lennard-Jones parameters σ and ε . The Lennard-Jones potential

$$U_{\text{LJ}}(r) = 4\varepsilon \left[\left(\frac{\sigma}{r} \right)^{12} - \left(\frac{\sigma}{r} \right)^6 \right] \quad (2.9)$$

describes both the short range Pauli repulsion due to overlapping electron orbitals and the long range van der Waals attraction in a computationally simple form. The shape of the potential is illustrated in figure 2.1. The other intermolecular potential term in equation 2.8 describes the electrostatic interaction.

A general form for an intramolecular force field U_{intra} includes terms for covalent bonds, covalent angles and torsional angles. Each of these might be modelled with harmonic potentials of the form

$$U(r) = k(r - r_0)^2 \quad (2.10)$$

where k is a force constant and r_0 an equilibrium position, or Morse potentials of the form

$$U(r) = D(1 - \exp(-\rho(r - r_0)))^2. \quad (2.11)$$

where D is a potential well depth. The Morse potential is a better approximation for molecular structure as it explicitly accounts for the effects of bond breaking and anharmonicity.

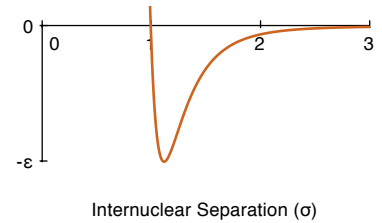


Figure 2.1: The shape of the Lennard-Jones potential describing intermolecular interaction.

2.1.3 Approximations

In sections 2.1.1 and 2.1.2 we discussed the approximations involved in the numerical method and force field definition. In any computer simulation, there are other approximations we must consider.

The simulated system size, even on the most powerful computers, must be orders of magnitude smaller than that of the experimental system.⁷ The effect of finiteness at the boundary of the system is handled using *periodic boundary conditions* (PBCs).

A cubic box is set up containing the collection of molecules, and these are replicated through space to form an infinite lattice. As an atom moves in the primary box its image in each replica box moves in the same way, and when one atom leaves an image enters the opposite face to take its place.

⁷ Thijssen, 2007, p199.

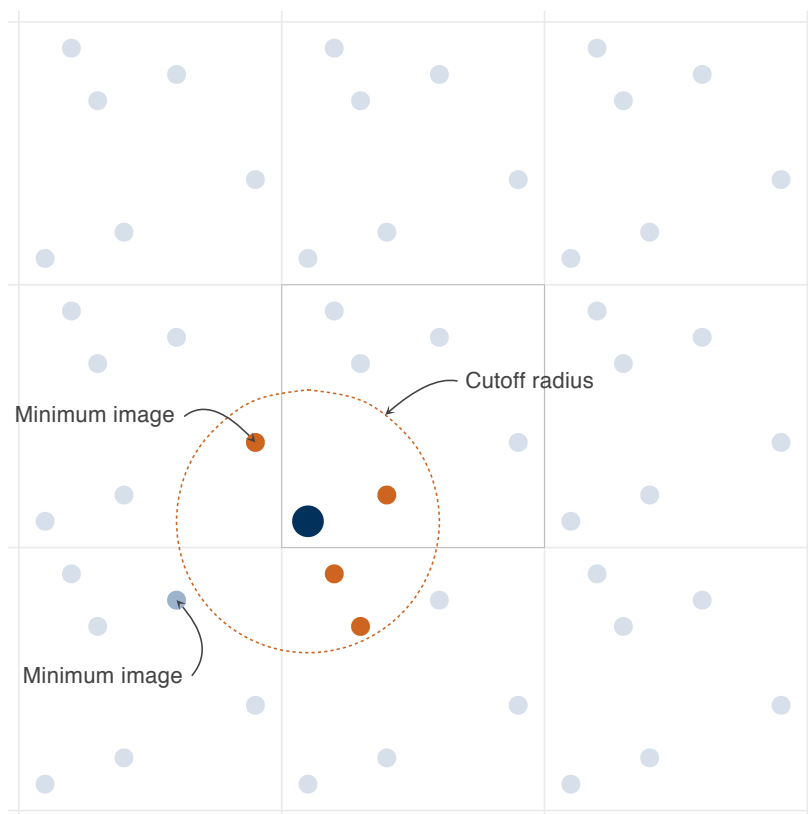


Figure 2.2: A 2D representative system, showing the simulation box (centre) and the nearest PBC image boxes, each containing images of the simulated particles.

For a given particle (dark blue), only interactions with the nearest image of each *other* particle are counted. Moreover, only those within the cutoff radius (orange) are included.

As well as remembering that we are only modelling pairwise interactions, we must also note that in considering a system with PBCs, we should sum over each copy of each atom in the same configuration, extending to infinity. This is obviously impossible. However, as the intermolecular force field falls off quickly, distant image atoms contribute negligibly. We thus apply the *minimum image* convention, choosing only the nearest copy of each atom to contribute.

Furthermore, we apply a *force cutoff* at a set radius, such that only atoms within this separation will be felt. This allows a huge

reduction in computational expense in calculating intermolecular interactions. Figure 2.2 shows PBCs, the minimum image convention and force cutoff schematically.

THE DURATION of the simulation, like the system size, is limited to being much smaller than any experimental setup. In order to make good time averages, it is typical to make on the order of 10^6 integration steps. For femtosecond time steps, this represents a simulated time on the order of nanoseconds (10^{-9} s). We therefore want the correlation time of the system to be significantly smaller than this.

2.1.4 Trajectory Analysis

Following a successful MD simulation, we have all the trajectory data — positions, velocities and forces on each particle — required to dig out the dynamical and structural properties we want to reveal. In the case of nitrate, I am particularly interested in the structure of the hydration shell around the anion and its dynamic reorientation behaviour.

Although the aqueous solution does not possess the translational order of a crystal, we may still characterise its structure by means of functions of the atomic positions, the simplest being the pair *radial distribution function* (RDF). This gives the probability of finding a specific pair of atoms⁸ at a distance r apart, relative to the probability expected for a random distribution of the same density. We define the pair distribution function by

$$g(r) = \frac{V}{N^2} \left\langle \sum_i \sum_{j \neq i} \delta(r - r_{ij}) \right\rangle \quad (2.12)$$

where i, j are atoms in the ensemble, r_{ij} is their separation, V is the simulation volume, N is the number of atoms and δ is the Kronecker delta.

The *spacial distribution function* (SDF) gives us a 3D distribution of a given atom in a specific coordinate system. In aqueous nitrate, for example, we may use an SDF to show the average location of water hydrogens around the nitrate solute.

The simplest dynamic information we can take from the trajectories is the *mean squared displacement* of a particular molecule. As the molecule travels through the liquid, it collides with other molecules in a Brownian translational motion. The mean squared displacement $\langle r^2 \rangle$ of a particle is proportional to the time elapsed, in the form

$$\langle r^2 \rangle = 6Dt + c \quad (2.13)$$

where the proportionality coefficient D , obtained in this manner, is called the diffusion coefficient.

WE OBTAIN FURTHER DYNAMIC INFORMATION about the system

⁸ For example, an oxygen atom in nitrate and a hydrogen in water.

from *time correlation functions* (TCFs). For a given molecular vector $\mathbf{n}(t)$, the TCF is determined as

$$c(t) = \frac{\langle \mathbf{n}(t_0) \cdot \mathbf{n}(t_0 + t) \rangle}{\langle \mathbf{n}(t_0)^2 \rangle} \quad (2.14)$$

where the average is taken over all molecules of the chosen type and initial times as part of a continuous trajectory.⁹

The *second-order* TCF is given by

$$c_2(t) = \frac{\langle L_2(\mathbf{n}(t_0) \cdot \mathbf{n}(t_0 + t)) \rangle}{\langle L_2(\mathbf{n}(t_0)^2) \rangle} \quad (2.15)$$

where the second-rank Legendre polynomial $L_2(x)$ is

$$L_2(x) = \frac{1}{2}(3x^2 - 1). \quad (2.16)$$

This second-order TCF will be especially useful when looking at the reorientation of the nitrate anion, that is when $\mathbf{n}(t)$ is a specified molecular vector, as it decays at the same rate as the ultrafast IR spectroscopy decay.^{10,11} We find the time constant τ for such a decay by fitting the TCF to an exponential function of the form in equation 1.1.

For aqueous nitrate, I'll be looking to analyse TCFs of molecular vectors and angular velocities to describe the reorientation of the molecule.

2.1.5 Jump Models

As mentioned in section 1.2, the traditional description of the dynamics of water molecules has been based on Debye rotational diffusion. Evidence from recent experimental work and results from MD simulations suggest that this behaviour might be better described by a model of picosecond reorientation by large angular jumps. In these jumps, a water O-H bond trades one H-bond acceptor for another.¹² Such jump behaviour has also been observed in the reorientation of anions in hydration shells.¹³

This exchange process can usefully be viewed as a chemical reaction, forming and cleaving H-bonds between the molecule and its environment.¹⁴ As such, we can describe the with an Arrhenius equation, describing the dependence of the reaction rate r on temperature T as

$$r = Ae^{-E_a/kT} \quad (2.17)$$

where k is the Boltzmann constant, E_a is the activation energy and A is a pre-exponential factor. Using TCFs to derive $r = \tau^{-1}$ for each simulated temperature T , we can obtain an effective activation energy E_a for the mechanism.

⁹ Allen and Tildesley, 1989, §6.3.

¹⁰ See section 1.3 for experimental details.

¹¹ Laage et al., 2011.

¹² Laage et al., 2011.

¹³ Laage and Hynes, 2007.

¹⁴ Laage, 2006.

2.2 Quantum Chemistry

Electrons are very light particles, so classical mechanics cannot accurately describe the electronic structure of atoms and molecules, even qualitatively.¹⁵ We need quantum mechanics.

¹⁵ Jensen, 2006, §3.

We know that all information about a given quantum mechanical system is stored in its wave function Ψ . In quantum chemistry, to find important physical properties of the system we aim to solve the stationary Schrödinger equation

$$H\Psi = E\Psi. \quad (2.18)$$

The Schrödinger equation can only be solved analytically in a few cases, with at most one electron. In all other cases, we must use computers to provide an accurate description.¹⁶

¹⁶ This is known as the *many-electron* problem.

Of course, it is possible to integrate numerically with discretising methods but in order to get a realistic electronic structure we would need all variables of the nuclei and electrons at a large number of grid points. This would require unfeasibly high computer time and storage.¹⁷ Approximation is required.

¹⁷ Thijssen, 2007, §4.

THE BORN-OPPENHEIMER APPROXIMATION is a key tool in solving the many-electron Schrödinger equation, by which the large mass difference between electrons and nuclei justifies neglect of the coupling between their respective motions.¹⁸ We solve the electronic part of the equation with the nuclei clamped in position as parameters. This gives us a potential energy surface which we then use to solve for the nuclear motion.

¹⁸ Griffiths, 2003, §10.

The electronic Schrödinger equation is then the biggest computational problem, and sophisticated tools exist for solving it. I'll be employing methods based on two families of such tools, Hartree-Fock and density functional theory.

2.2.1 Hartree-Fock

Hartree-Fock (HF) is an *ab initio* method, that is it makes no reference to empirical data. It makes use of the variational principle, which states that all approximate wave functions have energies greater than or equal to the exact energy, with the equality only holding for the exact wave function.¹⁹

¹⁹ Griffiths, 2003, §7.

We start with a trial function for the system wave function: a product of the electron spin-orbitals

$$\Psi(\mathbf{r}_1, \mathbf{r}_2, \dots, \mathbf{r}_N) = \chi_1(\mathbf{r}_1)\chi_2(\mathbf{r}_2) \dots \chi_N(\mathbf{r}_N) \quad (2.19)$$

as is the solution in the case of an independent particle Hamiltonian. However, as electrons are fermions the system wave function must be antisymmetric, satisfying the Pauli exclusion principle. This requirement is met by arranging the orbitals in a Slater determinant²⁰

²⁰ Thijssen, 2007, §4.4.

$$\Psi(\mathbf{r}_1, \mathbf{r}_2, \dots, \mathbf{r}_N) = \frac{1}{\sqrt{N!}} \begin{vmatrix} \chi_1(\mathbf{r}_1) & \chi_2(\mathbf{r}_1) & \cdots & \chi_N(\mathbf{r}_1) \\ \chi_1(\mathbf{r}_2) & \chi_2(\mathbf{r}_2) & \cdots & \chi_N(\mathbf{r}_2) \\ \vdots & \vdots & \ddots & \vdots \\ \chi_1(\mathbf{r}_N) & \chi_2(\mathbf{r}_N) & \cdots & \chi_N(\mathbf{r}_N) \end{vmatrix}. \quad (2.20)$$

The Slater determinant is the simplest antisymmetric linear combination of Hartree products. It describes N electrons occupying N orbitals without specifying which electron is in which orbital. By taking a single Slater determinant as our trial function we neglect the individual electron-electron repulsions, including them only as an average potential.²¹

²¹ Jensen, 2006, §3.2.

ARMED WITH A TRIAL FUNCTION, the next task is to minimise the wave function. The result of this is to derive the Hartree-Fock pseudo-eigenvalue equations

$$F_i \psi_i = \epsilon_i \psi_i \quad (2.21)$$

where ψ_i are a set of one-electron wave functions, the Hartree-Fock molecular orbitals. The Fock operator F_i is defined by

$$F_i = h_i + \sum_j^N (J_j - K_j) \quad (2.22)$$

where h_i is the core Hamiltonian containing the kinetic energy of the electron and its electrostatic attraction to the nuclei, J_j is the Coulomb operator describing the repulsion from the other electrons and K_j is the exchange operator, a consequence of the asymmetry of the wave function.²²

²² Jensen, 2006, §3.3.

Solving the Hartree-Fock equations yields an infinite spectrum of results. To find the ground state, we take the lowest N eigenstates of this spectrum as the new spin-orbitals of the electrons. These are then used to build a *new* Fock operator which is diagonalised again, and the procedure is repeated until sufficiently converged. The set of solutions are known as self-consistent field (SCF) orbitals.²³

²³ Thijssen, 2007, §4.5.

The HF method, by way of the exchange term in the Fock operator, takes into account the rule that prevents parallel spin electrons (known as *Fermi correlation*) but not the dynamic correlation of electrons in motion (*Coulomb correlation*). The method thus tends to overestimate the electron-electron repulsion.²⁴

²⁴ Jensen, 2006, §4.

Other techniques such as Møller-Plesset perturbation theory are designed to improve on HF by addressing the electron correlation.

2.2.2 Density Functional Theory

Density functional theory (DFT) has been widely-used in electronic structure calculations for solids, and the approach is now popular

for atoms and molecules due to its relatively low computational cost for high accuracy results.²⁵

The heart of DFT is the Hohenberg-Kohn theorem. This states that given any ground state particle density function $n_0(r)$ we can calculate the unique²⁶ corresponding ground state wave function. That is, the wave function is a *functional* of the density function

$$\Psi_0(\mathbf{r}_1, \mathbf{r}_2, \dots, \mathbf{r}_N) = \Psi_0[n_0(r)]. \quad (2.23)$$

This means that all ground state observables are functionals of the density too. The density has been promoted from one observable among many to the key variable from which expectation values of all other observables \hat{O} can be found²⁷ in the form

$$O_0 = O[n_0] = \langle \Psi[n_0] | \hat{O} | \Psi[n_0] \rangle. \quad (2.24)$$

The computational efficiency thus achieved is huge. The number of variables describing a wave function increases exponentially with the number of electrons; the density function has the same number of variables independent of the number of electrons.

The implicit detail that makes this conjuring trick possible is that the ground state wave function Ψ_0 must not only give the ground state but also minimise the energy.

There are then two problems to be solved for the reward of being able to determine all observables. First, to make good approximations of the kinetic energy $T[n]$ and electron-electron interaction $U[n]$ operators and second, to minimise the energy $E_v[n]$, given by

$$E_v[n] = T[n] + U[n] + V[n] = T[n] + U[n] + \int n(r)v(r)d^3r \quad (2.25)$$

for a given density function $n(r)$.

THE KOHN-SHAM EQUATIONS offer a method to minimise the energy, based on an approach of reintroducing single-particle wave functions while still accounting for many body effects. The ground state density is found by convergence in a *self-consistency cycle*.

The total energy is expressed as

$$E = T_s[\psi_i[n]] + U_H[n] + V[n] + E_{xc}[n] \quad (2.26)$$

where $T_s[\psi_i[n]]$ is the kinetic energy of a system of non-interacting electrons with the same density as our system. It depends on a full set of occupied orbitals ψ_i , each a functional of n . $U_H[n]$ is the Hartree electron-electron repulsion, $V[n]$ is the Coulombic nucleus-electron attraction and $E_{xc}[n]$ is the electron-electron *exchange-correlation* energy.

No explicit functional form for the exchange-correlation energy has been found, so a range of DFT methods have been designed

²⁵ Thijssen, 2007, §5.1.

²⁶ If the ground state is non-degenerate.

²⁷ Capelle, 2006, p7.

with different semi-empirical approximations. This is an active field of research.²⁸

The Local Density Approximation (LDA) assumes that the local density can be treated as a uniform electron gas.²⁹

The Generalised Gradient Approximation (GGA) include the first derivative of the density as a variable, taking into account non-uniformity in the electron density.³⁰ An example of GGA I will use for looking at nitrate is the BLYP method.

Hybrid functionals combine HF and DFT approximations for the exchange energy along with a functional for correlation. An example of a hybrid method I will use for looking at nitrate is B3LYP.

These DFT methods describe the electronic ground state. To study the electronically-excited states, time-dependent DFT is applied to determine the response of the electronic configuration to electromagnetic radiation. Time-dependent DFT is implemented with the linear-response approximation. Though this has limitations, this method is very useful in the study of extended systems.

2.2.3 Basis Sets

The basis set chosen for expansion of the molecular orbitals in a Hartree-Fock or Kohn-Sham calculation constitutes an inherent approximation. While a complete basis set — with an infinite number of functions — would give exact results, this is not possible in any numerical solution. The larger the basis set the better the accuracy, and certain choices of basis set may be better suited to certain orbitals.³¹

In quantum chemistry, basis sets are often linear combinations of atomic orbitals (LCAOs). The two widely-used basis functions are known as Slater-type orbitals (STOs) and Gaussian-type orbitals (GTOs) by reference to their shape in the radial coordinate.

Real atomic wave functions resemble STOs more closely, but GTOs are popular as they are easy to handle numerically.³²

The *minimum basis set* is the smallest possible, using only enough functions to contain the electrons of the atom. For example, in the case of hydrogen or helium this means a single *s*-function. For higher accuracy, doubling (DZ) or tripling (TZ) of the basis functions is introduced.³³ Polarisation and diffuse functions may also be added. Another option is to decrease the number of basis functions describing the core orbitals and increase the number of basis functions describing the valence orbitals — this is called a *split basis valence set*.³⁴

²⁸ Jensen, 2006, §6.5.

²⁹ Jensen, 2006, §6.5.1.

³⁰ Jensen, 2006, §6.5.2.

³¹ Jensen, 2006, §5.

³² Capelle, 2006, p39.

³³ They are also referred to as *zeta functions*, hence the *z*.

³⁴ Jensen, 2006, §5.2.

3

Computational Methods

3.1 Molecular Dynamics

I ran MD simulations on ensembles consisting of a single NO_3^- anion and a single K^+ cation in a solution of water using the M.DynaMix package. M.DynaMix is a modern simulation package which allows arbitrary mixture of rigid and flexible molecules.¹

¹ Lyubartsev and Laaksonen, 2000.

3.1.1 Force Fields

The intramolecular potential U_{intra} I used for flexible nitrate comprises of terms for covalent bonds and angles, and an improper dihedral angle between the four coplanar atoms. The aim of the MD simulations are not to simulate the vibrations directly on the level of classical dynamics, but rather to investigate the molecular reorientation. The harmonic potential is thus sufficiently accurate near equilibrium that I do not require the more computationally-expensive Morse potential.²

² See section 2.1.2 for a description of force field potentials.

The three N-O bonds were modelled with equilibrium lengths of 1.2676 Å and force constants $2196.6 \text{ kJ} \cdot \text{mol}^{-1} \cdot \text{Å}^{-2}$. The three O-N-O angles were modelled with an equilibrium of 120° and force constants $439.32 \text{ kJ} \cdot \text{mol}^{-1} \cdot \text{rad}^{-2}$ and the improper dihedral angle was modelled with equilibrium of 0° and a force constant $251.04 \text{ kJ} \cdot \text{mol}^{-1} \cdot \text{rad}^{-2}$. These intramolecular potentials were referenced from Jayaraman et al.³

³ Jayaraman et al., 2010.

The intermolecular force field U_{inter} used is as given in equation 2.8, comprising of Lennard-Jones and electrostatic interactions. The LJ coefficients and point charges for nitrate, taken from Vchirawongkwin et al., are listed in table 3.1.⁴

⁴ Vchirawongkwin et al., 2010.

	σ (Å)	ϵ ($\text{kJ} \cdot \text{M}^{-1}$)	q (e)
N	3.150	0.7113	1.118
O	2.850	0.8368	-0.706

Table 3.1: The U_{inter} parameters used for nitrate. LJ coefficients σ and ϵ , and point charges q .

Force field parameters for water and the potassium cation were as provided by the M.DynaMix database.

3.1.2 The System

The simulations were run in a constant volume and temperature (NVT) ensemble, using the Nosé-Hoover thermostat. I chose a concentration of 0.10 M to match the Aarhus experiment. This corresponded to the setting the pair of ions among 550 water molecules.

In order to evaluate temperature dependence, simulations were run between 280 and 360 K at 10 K increments.

The cubic box size was chosen as a function of density, with realistic water densities used over the temperature range. These densities, provided by NIST, are cited in table 3.2.⁵

T (K)	ρ (g/ml)
280	0.99991
290	0.99880
300	0.99656
310	0.99338
320	0.98943
330	0.98479
340	0.97954
350	0.97373
360	0.96740

⁵ Lemmon et al., 2011.

Table 3.2: The density ρ of water at temperature T , taken from NIST Chemistry WebBook. Lemmon et al., 2011.

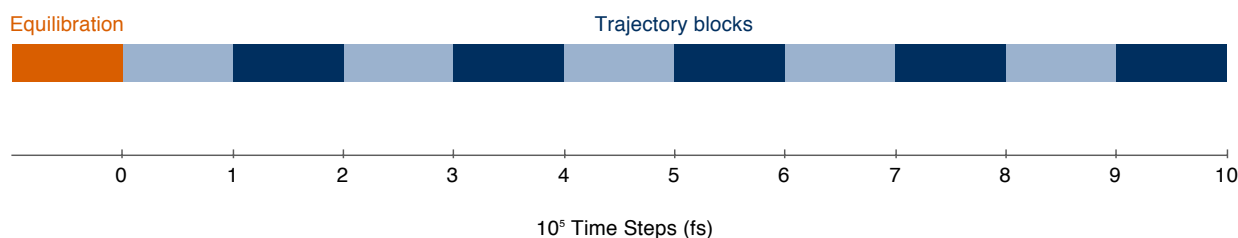
The simulations employed periodic boundary conditions with the minimum image convention and a cutoff radius of 10 \AA .⁶

⁶ See section 2.1.3

3.1.3 Numerical Integration

M.DynaMix uses the leapfrog Verlet integration method.⁷ I chose a time step of 1 fs. The ensembles were first equilibrated for 10^5 steps (100 ps) and then sampled for 10^6 steps (1 ns). M.DynaMix employs a double time step technique, whereby forces due to fast intramolecular and short-range ($< 5 \text{ \AA}$) intermolecular interactions are recalculated at a shorter time step, in this case 0.1 fs.

⁷ Lyubartsev and Laaksonen, 2000.



The positions, velocities and forces on each atom were recorded every 50 fs, and I used the M.DynaMix `trana1` tool to analyse RDFs, SDFs, mean squared displacements and TCFS as described in section 2.1.4.

Figure 3.1: The ensembles were equilibrated for 10^5 steps (100 ps) and sampled for 10^6 steps (1 ns).

3.2 Quantum Chemistry

Electronic structure calculations were performed using the Gaussian 03 software package.⁸ I calculated geometry optimisations and vibrational frequencies on ground state nitrate-water complexes.

⁸ Frisch et al., 2004.

A host of different initial geometries were chosen for small complexes of nitrate and water in order to locate minima in the potential, along with some symmetry-constrained structures for comparison. To obtain realistic hydration shells, I wrote a tool to cut out such structures from the MD trajectories.⁹

⁹ See appendix A for details of the Cutout tool.

Gaussian computes vibrational frequencies by determining the second derivatives of the energy with respect to the Cartesian nuclear coordinates and then transforming these to mass-weighted coordinates. This transformation is only valid at a stationary point, so the geometry optimisation must be successful.

3.2.1 Methods and Basis Sets

For the small complexes, I looked at four levels of theory: *ab initio* using HF, Møller-Plesset using MP2, DFT with the generalised gradient approximation (GGA) using BLYP and hybrid functionals using B3LYP.

I used the GTO-based 6-311G(d,p) basis set, with polarisation functions. For the smaller complexes I also used the AUG-cc-pVTZ basis set: Dunning's correlation consistent basis sets with triple zeta functions, augmented with diffuse functions.¹⁰

¹⁰ See section 2.2.3 for a discussion of basis sets.

For the hydration shell structures, I made calculations on the ground state using DFT methods and on the electronically-excited states using linear-response time-dependent DFT. However, I note that the time-dependent method only approximately describes the charge-transfer-to-solvent (CTTS) excitation.

4

Results & Discussion

4.1 Molecular Dynamics

I ran MD simulations, as described in section 3.1, on a canonical ensemble of water molecules with a single potassium nitrate ion pair. The concentration in each of these simulations matched that of the Aarhus experimental setup at 0.1 M.

These simulations will enable us to characterise the aqueous solution and the solvation of nitrate, and form a basis for studying the mechanisms behind the symmetry breaking in the asymmetric stretch modes and the reorientation motion.

The trajectories were analysed for structural and dynamic information which might reveal the mechanisms behind nitrate reorientation behaviour.

4.1.1 Structure

I first looked at the structure of the hydration shells that surround the nitrate molecule in solution.

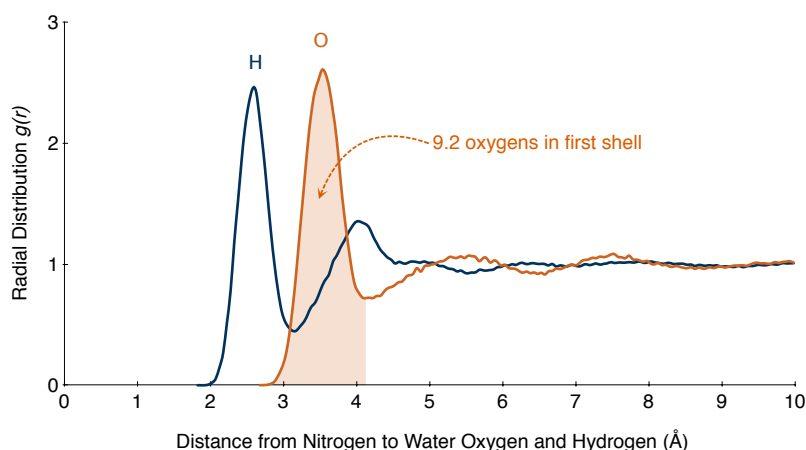


Figure 4.1: The RDF at 300 K of hydrogen (dark blue) and oxygen (orange) from the nitrogen atom at the origin. The shaded area (light orange) shows an integrated distribution of 9.2 oxygens up to the minimum after the first peak.

In figure 4.1 we have RDFs showing the distribution of water molecules around the nitrate anion at 300 K, with the origin set at the central nitrogen atom. We see a well-defined peak of water hydrogen atoms at a distance of ~ 2.6 Å and of water oxygen atoms

at $\sim 3.5 \text{ \AA}$ indicating the first hydration shell. A second hydrogen peak at $\sim 4.0 \text{ \AA}$ corresponds to the other hydrogen in the water molecule, after which the sampling is a little noisy.

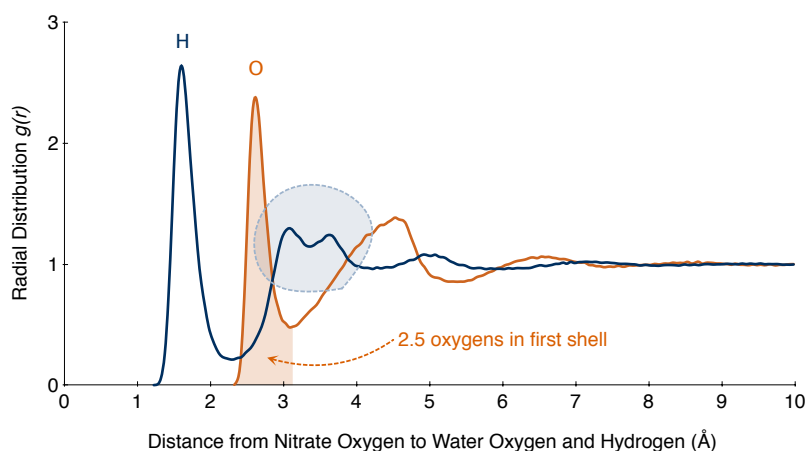


Figure 4.2: The RDF at 300 K of hydrogen (dark blue) and oxygen (orange) from the three nitrate oxygen atoms at the origin. The shaded area (light orange) shows an integrated distribution of 2.5 oxygens up to the minimum after the first peak. The geometric origin of the circled double peak (light blue) is illustrated in figure 4.3.

Consistent with this, figure 4.2 shows an RDF of the same water oxygen and hydrogen atoms from the perspective of the three nitrate oxygens. We see the strong peak of water hydrogen atoms at a distance of $\sim 1.6 \text{ \AA}$ and water oxygen atoms at $\sim 2.5 \text{ \AA}$. The smaller double peak in the hydrogen atoms between $\sim 3.0 \text{ \AA}$ and 3.7 \AA is due to secondary, non-H-bonded collocations in the bonded molecules, shown schematically in figure 4.3.

The cumulative distributions shown under the oxygen peaks to the first minimum in figures 4.1 and 4.2 show an average of 9.2 oxygen atoms in the first shell around each nitrogen atom, and 2.5 around each of the three nitrate oxygens. This suggests a coordination of two to three H-bonded water molecules around each of the nitrate anion's three oxygen atoms.

The maxima and minima of these RDFs compare well with the results of Laaksonen and Kovacs¹, who found up to 8 water molecules coordinating the oxygen atoms of nitrate.

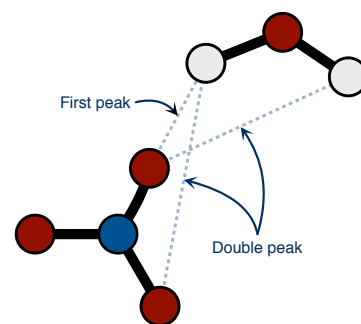


Figure 4.3: A schematic describing the origin of the RDF peaks in figure 4.2. The first corresponds to the H-bond and the secondary double peak corresponds to other collocated oxygen-hydrogen pairs.

¹ Laaksonen and Kovacs, 1994

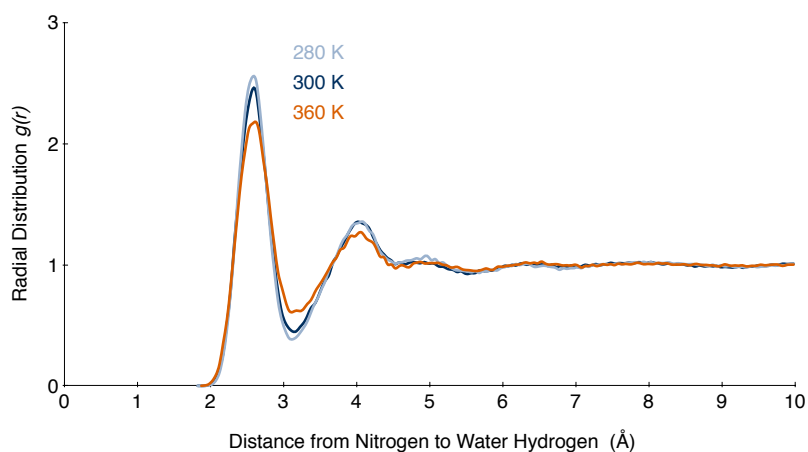


Figure 4.4: The RDF of water hydrogen from the nitrogen atom at 280 K (light blue), 300 K (dark blue) and 360 K (orange). We see a consistent structure across the temperature range.

THE TEMPERATURE DEPENDENCE of the hydration shell structure is shown in the RDFs of figure 4.4, which plot the nitrogen to water hydrogen distribution. The 300 K nitrogen-hydrogen function (dark blue) from figure 4.1 is repeated, and added are the lowest and highest temperature simulations, 280 K (light blue) and 360 K (orange). We see that the location of the well-defined first and second peaks does not change across the temperature range, but that both the maximum and minimum are more prominent with decreasing temperature.

The integrated distribution of oxygen atoms in the first shell decreases only from 9.2 at 280 K to 9.1 at 360 K, suggesting that the water coordination structure is consistent across the temperature range.

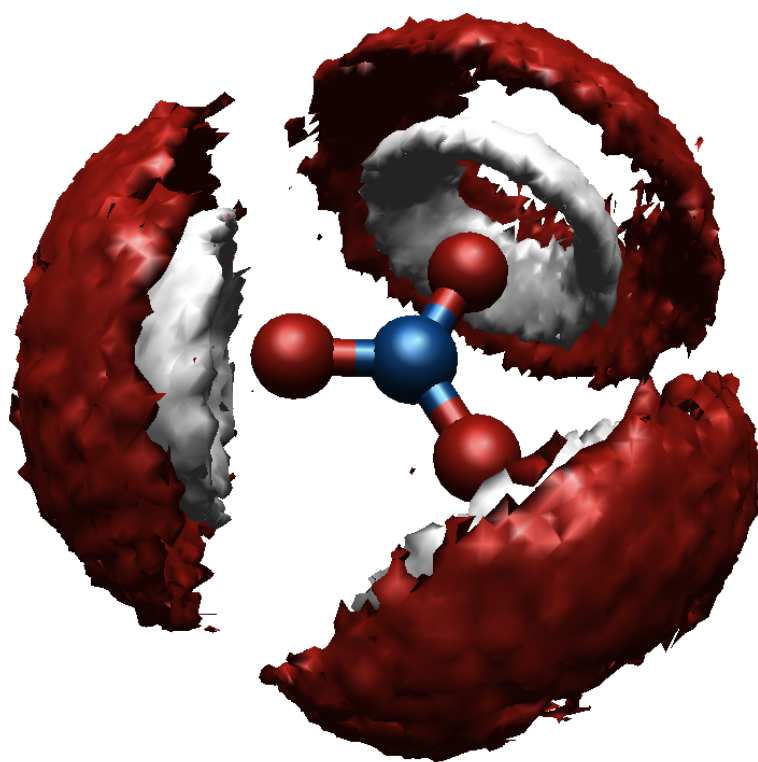


Figure 4.5: The SDF of water oxygen (red) and hydrogen (white) around the nitrate ion at 300 K.

Figure 4.5 shows the 3D spacial distribution at 300 K of water hydrogen and oxygen atoms around the nitrate ion, indicating the average locations of water molecules in the first hydration shell.

The picture is consistent with the RDF peaks of figures 4.1 and 4.2, and furthermore we also see cylindrical symmetry around each of the three oxygen atoms, with a preferred angle of between 30° and 75° from the nitrate N-O bond to the H-bonded water molecule O-H bond.

No discernible change in the SDF is visible across the temperature range from 280 K to 360 K, so I disregard those plots.

The RDF of the single potassium cation from the nitrogen atom is in figure 4.6. The plot is noisy, as it only samples one atom pair.

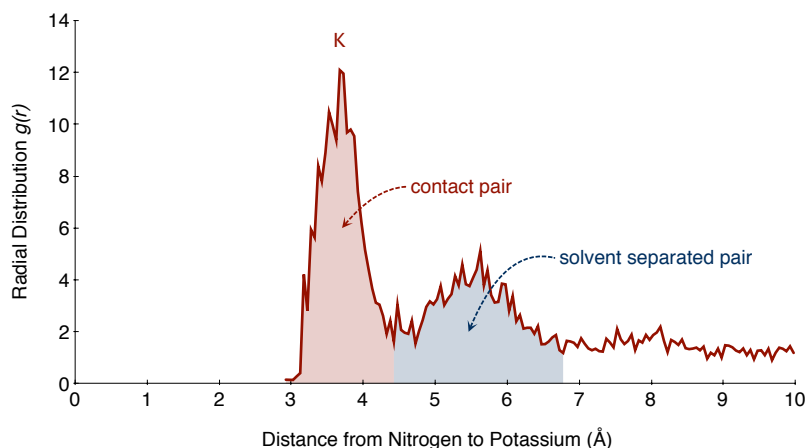


Figure 4.6: The RDF at 300 K of the lone potassium cation from the nitrogen atom.

However, it suggests that the cation spent $\sim 8\%$ of the simulation time coordinated between ~ 3 to 4 \AA and $\sim 12\%$ of the time in a solvent separated state between ~ 5 to 7 \AA .

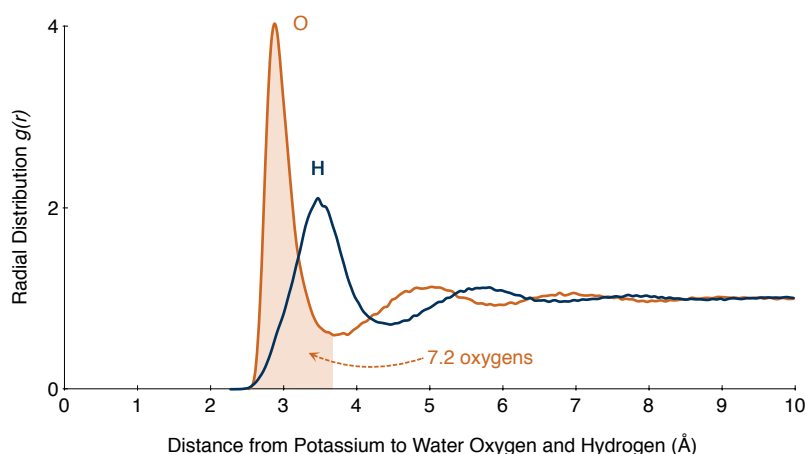


Figure 4.7: The RDF at 300 K of water oxygen and hydrogen atoms from the potassium cation.

Figure 4.7 is the RDF of water oxygen and hydrogen atoms from the potassium cation. We see well-defined peaks, with oxygen peak closer than hydrogen in contrast to the nitrate coordination. The oxygen coordination number 7.2 agrees well with previous results in *ab initio* MD of 6.75 by Ramaniah and 7 by Nguyen and Adelman.²

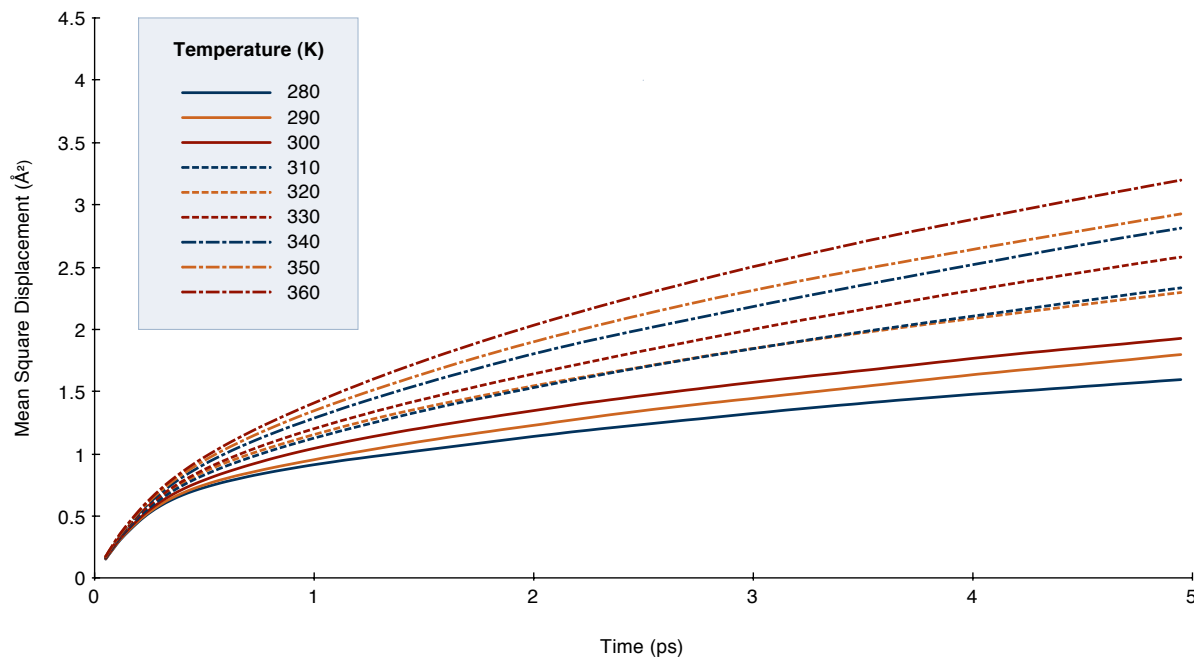
² Ramaniah et al., 1999

4.1.2 Dynamics

I first looked to obtain diffusion coefficients by measuring the mean squared displacement of the nitrate molecule over the simulated trajectories.³ Figure 4.8 shows the mean squared displacement of the nitrate molecule over 5 ps.

Figure 4.9 plots the diffusion coefficients over the temperature range from 280 K to 360 K, and these are listed in table 4.1. We see that the diffusion coefficient increases linearly with temperature.

³ See section 2.1.4 for a theoretical background.



The datapoint at 310 K lies off the line, which is likely erroneous.

We can compare this result to the MD result of $D = 2.5$ at 315 K by Laaksonen and Kovacs, at much higher concentration and the self-diffusion coefficient $D \approx 2.3$ of water at 300 K.^{4,5}

T (K)	D ($10^{-5}\text{cm}^2\text{s}^{-1}$)
280	0.73
290	0.97
300	1.09
310	1.75
320	1.65
330	2.20
340	2.62
350	2.83
360	3.48

I TURNED NEXT to reorientation dynamics. As described in section 2.1.4, the second-rank TCF of molecular orientation is a principle description of its dynamics and can be directly linked to the anisotropy decay of IR spectroscopy data.

I looked at the orientation of three perpendicular molecular vectors: the vector \mathbf{i} along an N-O bond, the vector between the two other oxygen bonds \mathbf{j} and the vector normal to the plane \mathbf{k} . These vectors, shown in figure 4.16, are fixed for each molecule through the trajectory.

The second-rank TCF of the normal \mathbf{k} vector at 300 K is shown

Figure 4.8: Mean squared displacement over 5 ps at 10 K temperature increments between 280 K and 360 K.

⁴ Laaksonen and Kovacs, 1994.

⁵ Tanaka, 1978.

Table 4.1: Diffusion coefficients of nitrate in water at 10 K temperature increments between 280 K and 360 K.

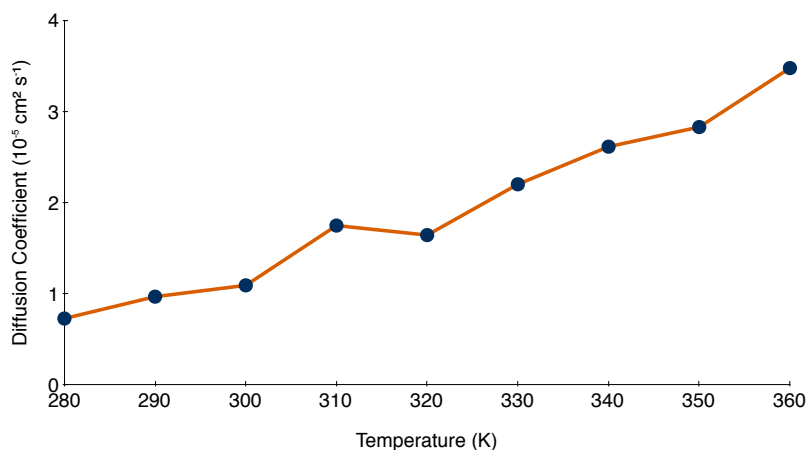
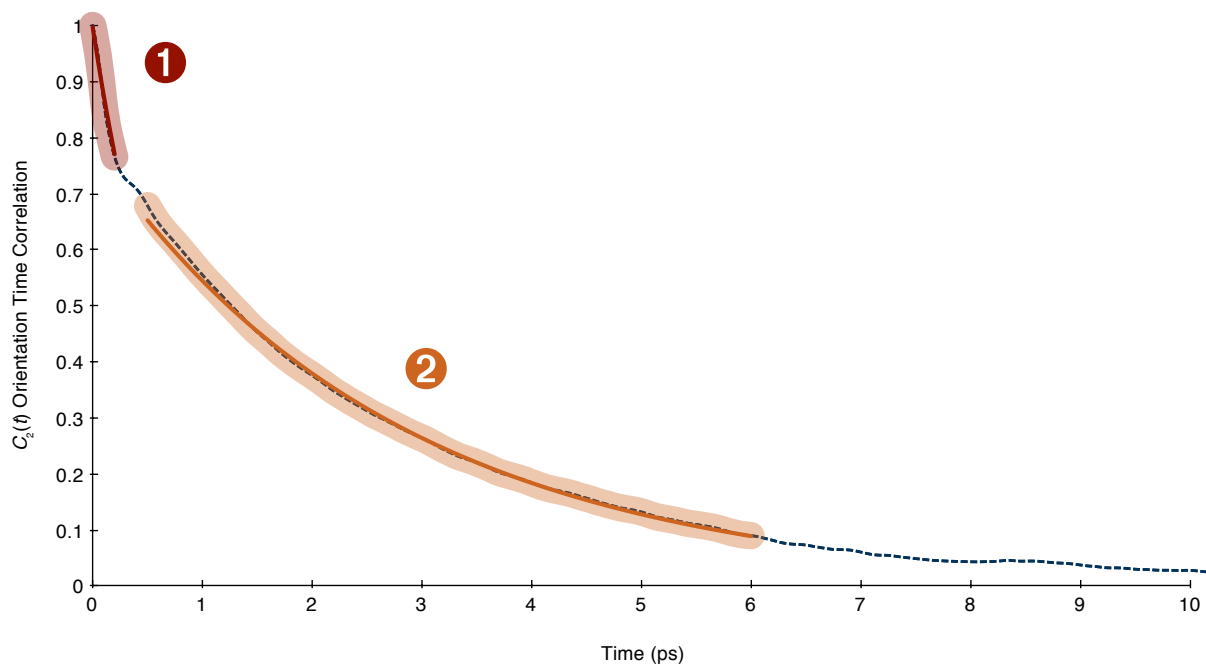


Figure 4.9: Diffusion coefficients of nitrate in water at 10 K temperature increments between 280 K and 360 K.

in figure 4.10. The nitrate reorientation proceeds successively at two different rates, due to different mechanisms. An ultrafast (sub-picosecond) partial reorientation (region ①) is followed by a slower full reorientation (region ②).

Following the description by Laage et al.⁶ of water reorientation, we explain the region ① decay as the nitrate anion's rotational motion, rapidly slowed by H-bonds in the hydration sphere.

⁶ Laage, 2006.



This *librational* motion results in an ultrafast (< 200 fs) reorientation as each nitrate N-O bond wobbles in a cone centred on the H-bond direction (see figure 4.11).

THE SLOWER DECAY of region ② dominates after around 500 fs, fol-

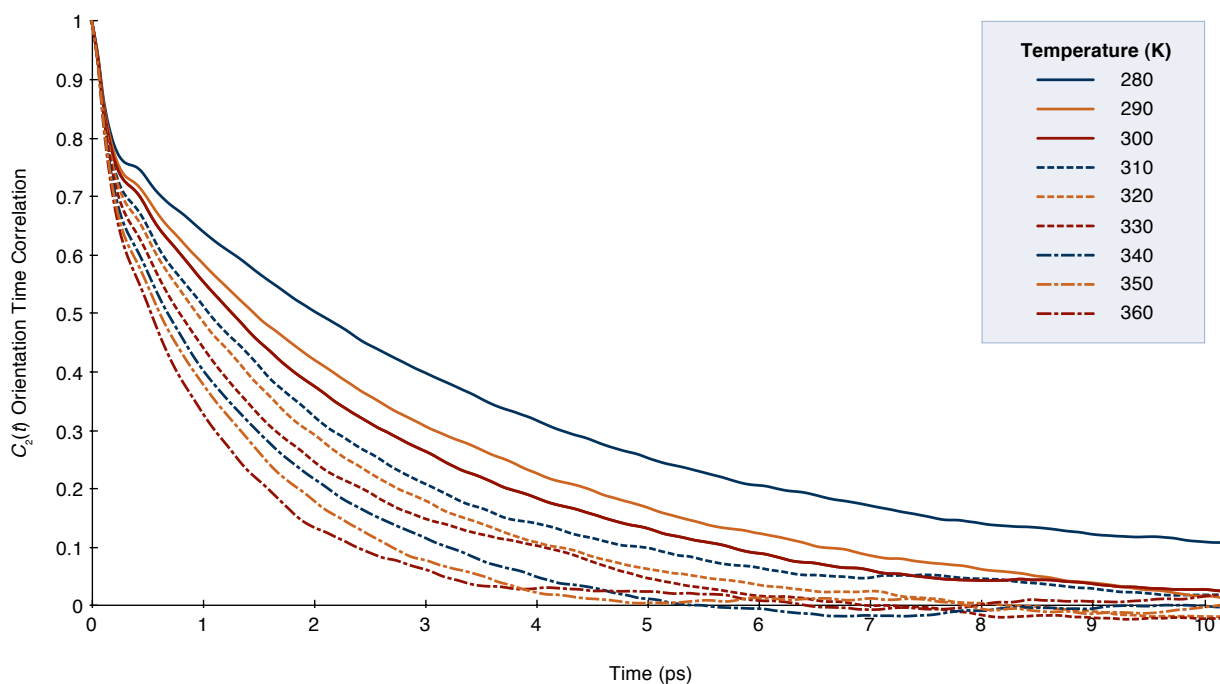
Figure 4.10: The second-rank TCF (dashed, dark blue) of the \mathbf{z} vector at 300 K. Two different regions proceed at different rates (red, ①) and (orange, ②), and these are fitted to standard mono-exponential decay functions (solid red and orange lines).

lowing a ‘bump’ joining the two regions, likely due to the transition to a different reorientation mechanism.

As described in section 2.1.5 recent experimental and theoretical evidence suggests a mechanism for picosecond reorientation involving sudden large angular jumps.⁷

Observations of frequent large-amplitude jumps in the trajectories of these MD simulations leads me to argue for the jump model in aqueous nitrate solution. Large jumps are observed to coincide with water molecules entering the hydration shell, forming H-bonds and over-coordinating a nitrate oxygen. Conversely, jumps are observed when a water molecule makes its own large rotation, breaking the nitrate H-bond and departing the hydration shell.

THE TEMPERATURE DEPENDENCE of the second-rank TCF of the normal \mathbf{k} vector is shown in figure 4.12, where we look at a range from 280 K to 300 K in increments of 10 K. We see the same ultrafast region ① and picosecond region ② at each temperature, though the difference between the reorientations is more pronounced at lower temperatures.



Up to ~ 3 ps, we see a consistent spacing in the TCFs. At each temperature, these were fitted to standard exponential decays, as described in section 2.1. The two dominant decays describing regions ① and ② are listed in table 4.2 and plotted in figures 4.13 and 4.14.

The time constants τ of both mechanisms decrease with increased temperature, describing faster reorientation. The picosecond decay ② at 330 K in figure 4.14 lies outside the linear trend,

⁷ Laage et al., 2011.

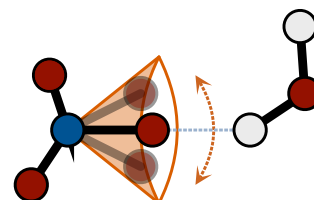


Figure 4.11: Librational motion. The nitrate bond wobbles in a cone centred on the H-bond direction.

Figure 4.12: The second-rank TCF of the \mathbf{z} vector at 10 K temperature increments between 280 K and 360 K.

possibly due to the non-exponential ‘bump’ in that TCF at around 4 ps.

The very high time constants at 280 K indicate that the solution is perhaps coming close to freezing out some degrees of freedom.

T (K)	τ_1 (ps)	τ_2 (ps)
280	0.89 ± 0.07	4.33 ± 0.06
290	0.82 ± 0.05	3.23 ± 0.03
300	0.78 ± 0.05	2.80 ± 0.05
310	0.72 ± 0.05	2.37 ± 0.09
320	0.70 ± 0.04	2.00 ± 0.00
330	0.65 ± 0.03	1.96 ± 0.01
340	0.60 ± 0.03	1.39 ± 0.11
350	0.57 ± 0.02	1.15 ± 0.07
360	0.54 ± 0.02	1.32 ± 0.13

Table 4.2: Fitted exponential decay constants for the second-rank TCF of the \hat{z} vector at 10 K temperature increments between 280 K and 360 K.

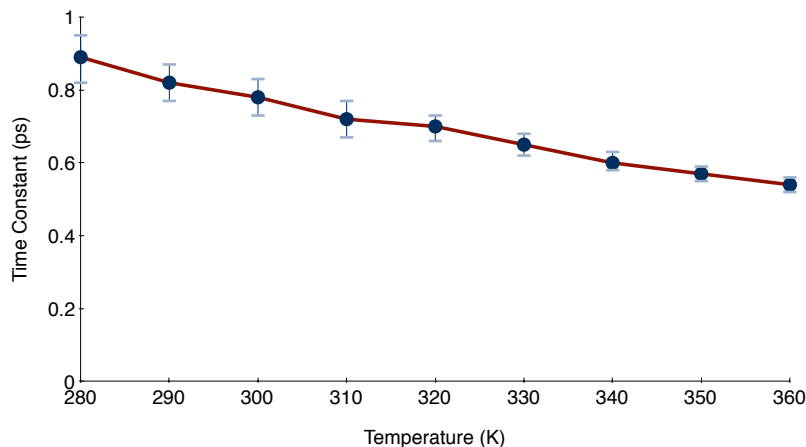


Figure 4.13: Time constants τ_1 fitted to the ultrafast motion at 10 K temperature increments between 280 K and 360 K.

The time constants for the picosecond reorientation ② showed some variation over the region when fitted to a mono-exponential function. I thus fitted these curves over two subregions, 1 to 5 ps and 2 to 6 ps. The results for τ_2 in table 4.2 are hence given as the median of these two values, which form the high and low errors.

THE ARRHENIUS EQUATION, as described in section 2.1.5, allows us to treat the reorientation mechanism as a chemical reaction, and so derive an activation energy E_a from the dependence of the reaction rate $r = \tau^{-1}$ on temperature.

For the picosecond rotation ②, the slope of the linear fit in figure 4.15 gives $E_a = 13.4 \pm 1.0 \text{ kJ} \cdot \text{mol}^{-1}$. We can compare this to a typical H-bond energy of 16 to 20 $\text{kJ} \cdot \text{mol}^{-1}$. The Boltzmann distribution states that 0.32% of the molecules have this energy at 280 K and 1.14% at 360 K.

I SEARCH FOR ANISOTROPY in the reorientation dynamics by com-

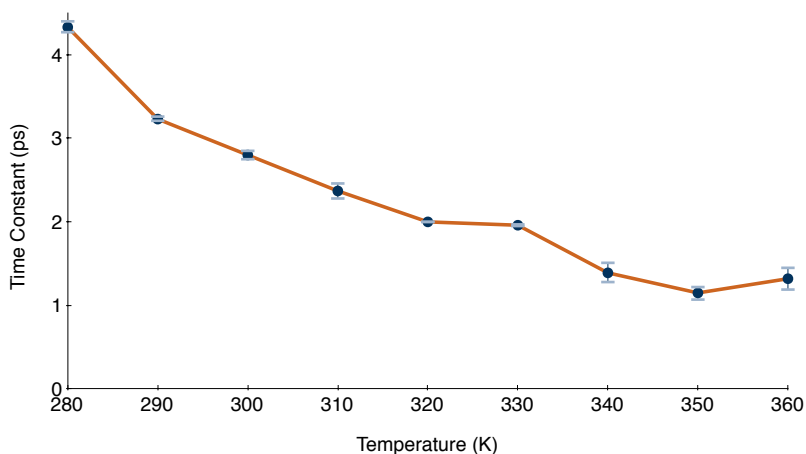


Figure 4.14: Time constants τ_2 fitted to the ultrafast motion at 10 K temperature increments between 280 K and 360 K.

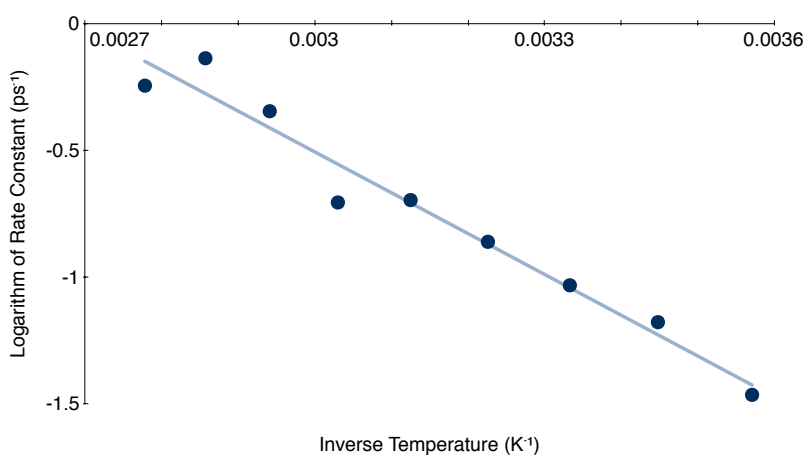


Figure 4.15: The Arrhenius plot of reaction rate $r = \tau^{-1}$ against inverse temperature T^{-1} . The activation energy E_a is derived from this slope.

paring the TCFs along the molecular vectors \mathbf{i} , \mathbf{j} and \mathbf{k} . Each of the TCF results presented so far have been for the vector \mathbf{k} , normal to the nitrate plane. How does this compare to the in-plane reorientation of \mathbf{i} and \mathbf{j} ?

In figures 4.17, 4.18 and 4.19 we see the TCFs for the three molecular vectors at temperatures of 280 K, 300 K and 360 K respectively. The fitted time factors τ are listed in table 4.3.

We see the same distinct regions ① and ② in each of the molecular vectors. At each temperature we see the ultrafast ① time constant is lower in \mathbf{k} than in \mathbf{i} and \mathbf{j} , indicating that libration is more constrained in the plane.

For the picosecond rotation there is only a significant difference between the vectors at 280 K, as shown by the graphs. Along with the diffusion results, this suggests that some degree of freedom may be frozen out at this temperature.

THE ANGULAR VELOCITY vector motion can also be measured using TCFs, and this is another area I checked for anisotropy. I sampled the angular velocity TCFs from higher-resolution trajectories,

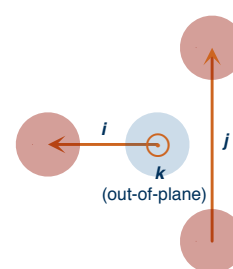
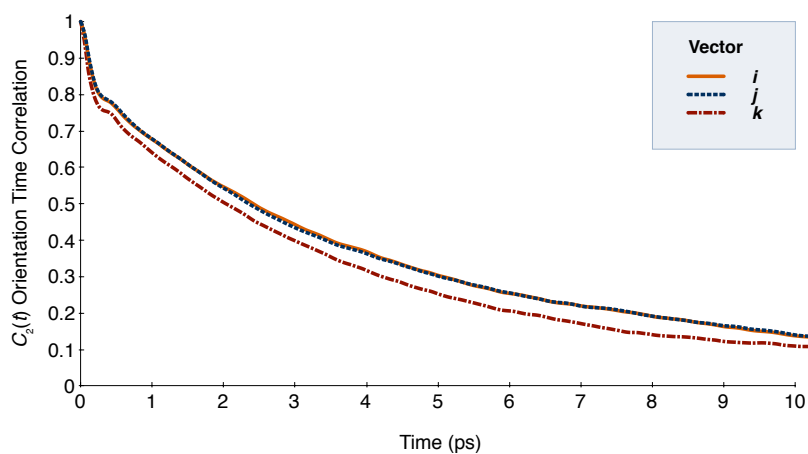
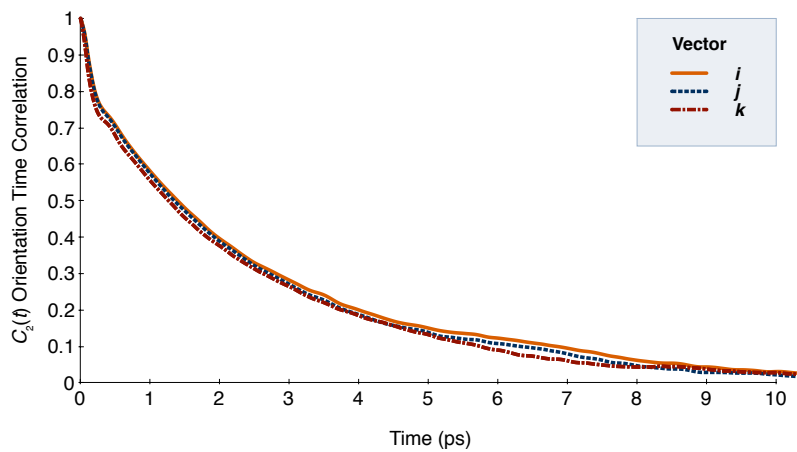
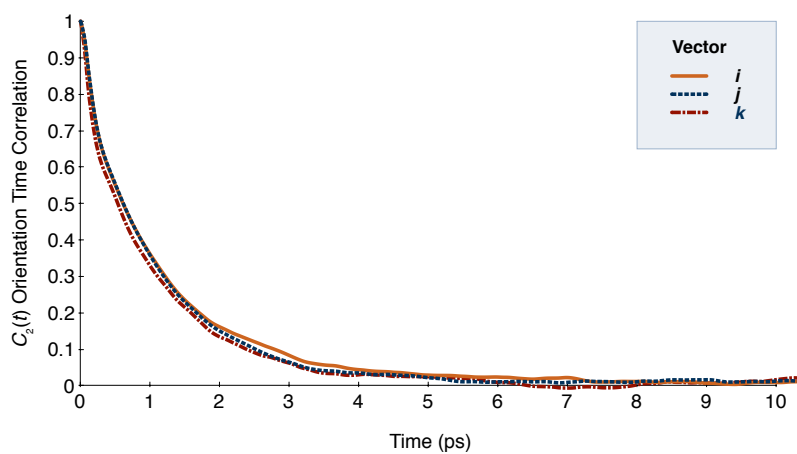


Figure 4.16: Molecular vectors.

Figure 4.17: Reorientation TCFs for the molecular vectors i , j and k at 280 K.Figure 4.18: Reorientation TCFs for the molecular vectors i , j and k at 300 K.Figure 4.19: Reorientation TCFs for the molecular vectors i , j and k at 360 K.

T (K)	$\mathbf{n}(t)$	τ_1 (ps)	τ_2 (ps)
280	i	1.08 ± 0.05	5.05 ± 0.13
280	j	1.09 ± 0.06	5.06 ± 0.24
280	k	0.89 ± 0.07	4.33 ± 0.06
300	i	0.91 ± 0.04	2.81 ± 0.10
300	j	0.93 ± 0.05	3.01 ± 0.16
300	k	0.78 ± 0.05	2.80 ± 0.05
360	i	0.66 ± 0.03	1.53 ± 0.13
360	j	0.66 ± 0.04	1.29 ± 0.07
360	k	0.54 ± 0.02	1.32 ± 0.13

Table 4.3: Fitted exponential decay constants for the second-rank TCF of the **i**, **j** and **k** molecular vectors at 280, 300 and 360 K, corresponding to the ultrafast ① and picosecond ② reorientations.

recording the configuration every 2 fs. I then averaged over 10 MD runs of 100 ps.

Figures 4.20, 4.21 and 4.22 show the angular velocity time correlation in the molecular axes defined by **i**, **j** and **k** respectively.

The anticorrelation seen between 0.2 and 0.3 ps corresponds to the constrained librational motion seen in region ① of the reorientation TCFs.

With this higher-resolution analysis, we see clearly that there is no anisotropy in the angular velocity of the three molecular vectors. The correlation is not distinguishable by axis.

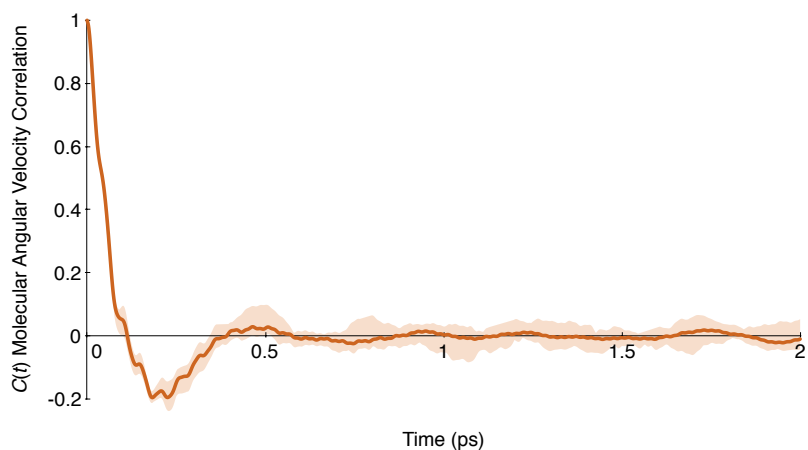


Figure 4.20: The angular velocity TCF in the molecular axes defined by *i* at 300 K.

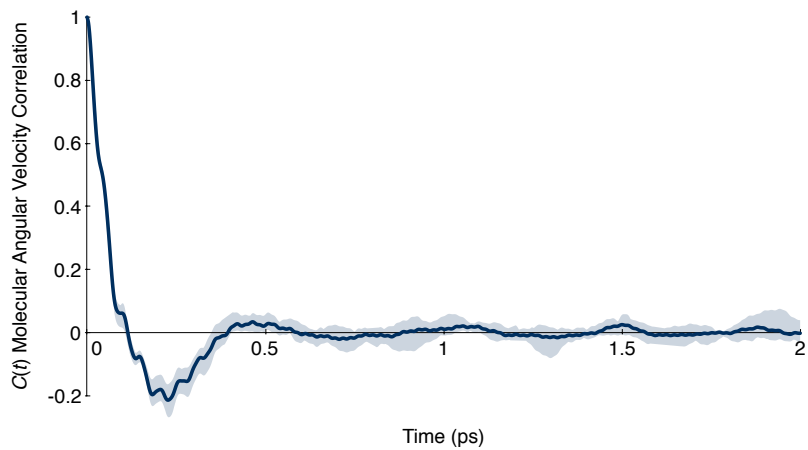


Figure 4.21: The angular velocity TCF in the molecular axes defined by *j* at 300 K.

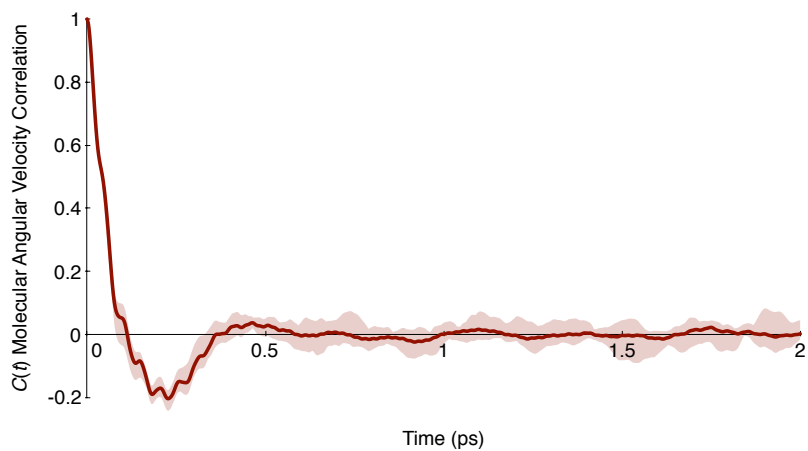


Figure 4.22: The angular velocity TCF in the molecular axes defined by *k* at 300 K.

4.2 Quantum Chemistry

Using the methods and software tools described in section 3.2, I made calculations to determine optimised geometries, electronic structure, vibrational modes and excited states of nitrate-water complexes.

Firstly, I optimised the geometry of the isolated nitrate molecule and observed the degenerate asymmetric stretch modes. Secondly, I looked at small complexes of nitrate with one and two water molecules to observe the simplest examples of symmetry breaking and to select and calibrate an appropriate combination of method and basis set. Finally, I applied the chosen method and basis set to hydration shells cut out from the MD simulations described in section 4.1. These hydration shell calculations should give good examples of the environment the nitrate molecule inhabits in aqueous solution.

4.2.1 The Isolated Anion

The bond lengths calculated for the isolated, geometry-optimised nitrate molecule using each combination of method and basis set are given in table 4.4. We see the D_{3h} symmetry in each case. I will be using the accurate but computationally-expensive MP2/AUG-cc-pVTZ level of theory as a reference in section 4.2.2, and we may note here that the B3LYP/6-311G(d,p) calculation makes an accurate (-0.1%) approximation to the geometry calculated at that level.

Method	Basis Set		N-O ₁	N-O ₂	N-O ₃
MP2	AUG-cc-pVTZ	*	1.2606	1.2606	1.2606
HF	AUG-cc-pVTZ		1.2205	1.2206	1.2206
BLYP	AUG-cc-pVTZ		1.2805	1.2806	1.2806
B3LYP	AUG-cc-pVTZ		1.2580	1.2581	1.2581
MP2	6-311G(d,p)		1.2593	1.2593	1.2593
HF	6-311G(d,p)		1.2206	1.2206	1.2206
BLYP	6-311G(d,p)		1.2826	1.2825	1.2825
B3LYP	6-311G(d,p)		1.2596	1.2595	1.2595

Table 4.4: Optimised bond lengths (in Å) for the isolated nitrate with each method and basis set. The reference MP2/AUG-cc-pVTZ is marked (*).

Figure 4.23 gives the frequencies of the degenerate asymmetric stretch modes ν_{3x} and ν_{3y} calculated with each combination. The frequencies calculated using the 6-311G(d,p) basis set are consistently higher than those using AUG-cc-pVTZ, by around 5%. The inclusion of diffuse functions in the AUG-cc-pVTZ basis set, are softening the vibrational modes.

The HF method approximates a higher frequency relative to the reference MP2 method. The BLYP and B3LYP methods approximate lower frequencies relative to MP2.

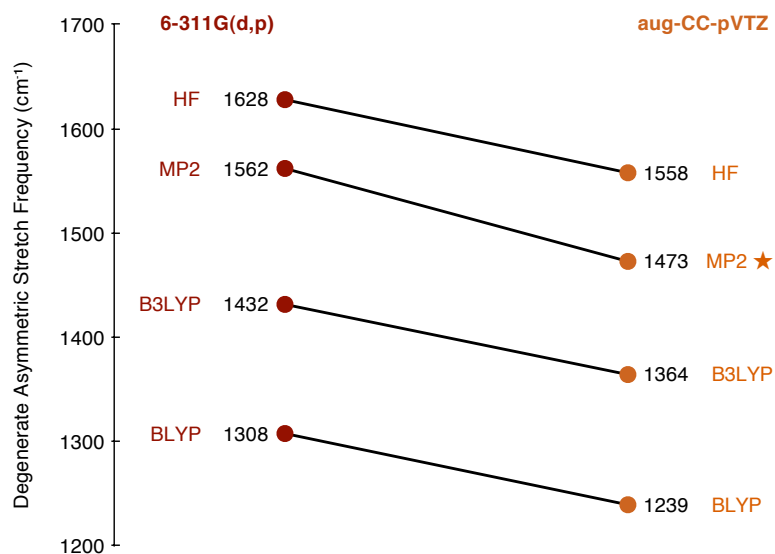


Figure 4.23: The frequencies (in cm^{-1}) of the degenerate asymmetric stretch modes ν_{3x} and ν_{3y} calculated by each combination of method and basis set. The reference MP2/AUG-cc-pVTZ is marked (*).

4.2.2 Small Complexes

To select and calibrate a method and basis set, I chose a few geometries of small complexes $[\text{NO}_3 \cdot (\text{H}_2\text{O})_n]^-$ with $n = 1, 2$.

For $[\text{NO}_3 \cdot \text{H}_2\text{O}]^-$ I found the global minimum to be a structure having C_{2v} symmetry, with the water molecule H-bonded to two of the nitrate oxygen atoms, shown in figure 4.24. I'll label this geometry ①.

Along with the global minimum I chose two other C_{2v} symmetry-constrained structures, with the plane of the water molecule perpendicular to the plane of the anion. The first, shown in figure 4.25, forms a H-bond with a single nitrate oxygen atom. The second, shown in figure 4.26, has the water such that a HO bond bisects the angle of two nitrate NO bonds. I'll label these structures geometry ② and ③, respectively.

THE SYMMETRY BREAKING effect is immediately apparent in the case of this small complex in figure 4.27. It shows the computed IR spectrum for the asymmetric stretch modes in $[\text{NO}_3 \cdot \text{H}_2\text{O}]^-$ geometry ①, alongside the computed spectrum for the isolated anion.

The single peak in the isolated state is replaced by a double peak, both *split* and *shifted* from its place.

Figure 4.28 is a schematic representation of the global minimum geometry ① computed using MP2/AUG-cc-pVTZ. The water molecule forms H-bonds to two of the nitrate oxygen atoms, both at a distance of $\sim 2.0 \text{ \AA}$. The presence of the water molecule distorts the nitrate, breaking its symmetry to C_{2v} . We see that two NO bonds with H-bonded oxygen atoms are longer than the third NO bond, and that the angle between the two H-bonded NOs is larger

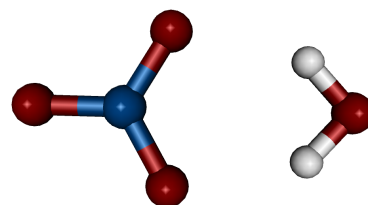


Figure 4.24: The $[\text{NO}_3 \cdot \text{H}_2\text{O}]^-$ global minimum, geometry ①.

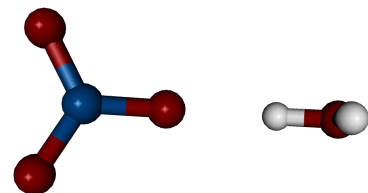


Figure 4.25: An $[\text{NO}_3 \cdot \text{H}_2\text{O}]^-$ symmetry-constrained structure, geometry ②.

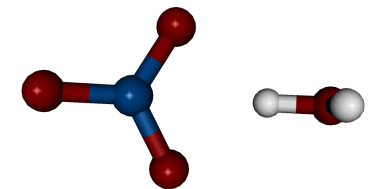


Figure 4.26: Another $[\text{NO}_3 \cdot \text{H}_2\text{O}]^-$ symmetry-constrained structure, geometry ③.

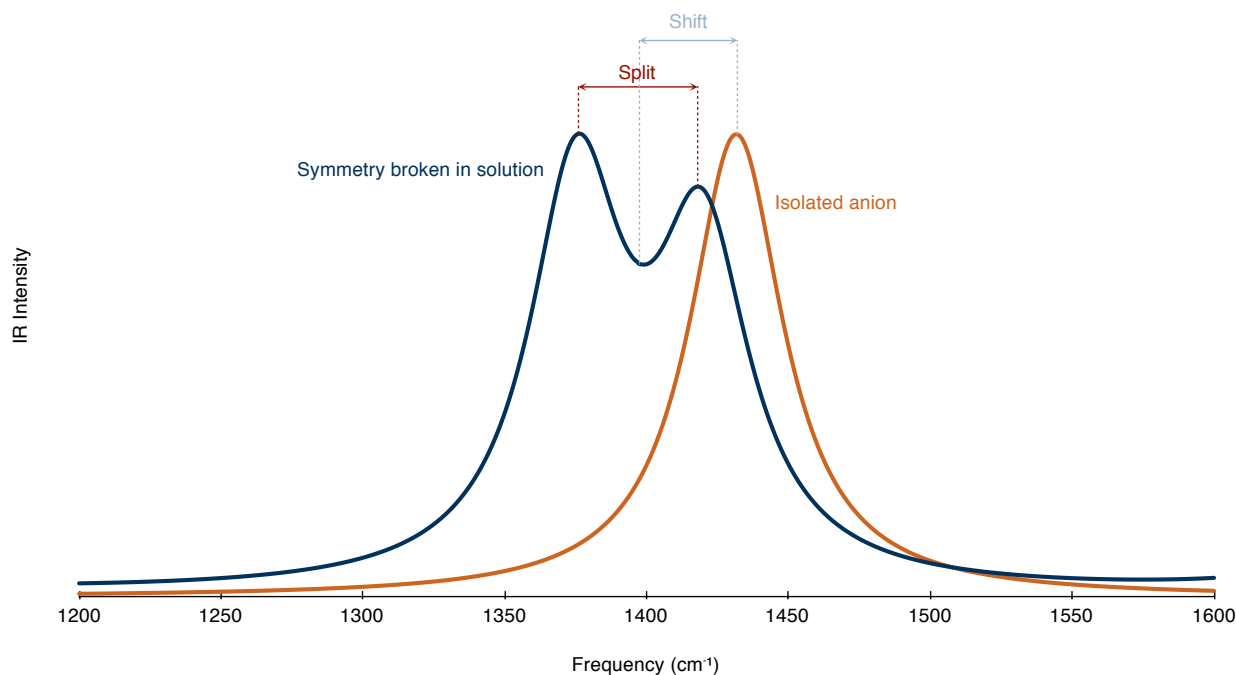


Figure 4.27: The simulated IR spectra of geometry ① (blue) alongside that of the isolated anion (orange).

than 120° .

THE ASYMMETRIC STRETCH SPLITS at each level of theory for $[\text{NO}_3 \cdot \text{H}_2\text{O}]^-$ geometries ①, ② and ③ are listed in figures 4.5, 4.6 and 4.7.

Method	6-311G(d,p)	AUG-cc-pVTZ
MP2	67.8217	★ 58.0769
HF	53.5617	40.9920
BLYP	81.7683	62.7177
B3LYP	73.6305	56.9563

Table 4.5: Asymmetric stretch splits by method and basis set in geometry ①. The reference MP2/AUG-cc-pVTZ is marked (★).

Method	6-311G(d,p)	AUG-cc-pVTZ
MP2	70.7713	★ 87.4053
HF	58.8211	30.4998
BLYP	57.9446	48.4644
B3LYP	54.8509	45.8271

Table 4.6: Asymmetric stretch splits by method and basis set in geometry ②.

The relative treatment of the splitting by each method and basis set can be seen more clearly in figures 4.29, 4.30 and 4.31. We see that the splitting using the 6-311G(d,p) basis set tends to be larger than that using the AUG-cc-pVTZ, by $\sim 20\%$ to 40% . We also see that the HF method makes lower approximations to the splitting than the reference MP2 and that BLYP and B3LYP make higher approxi-

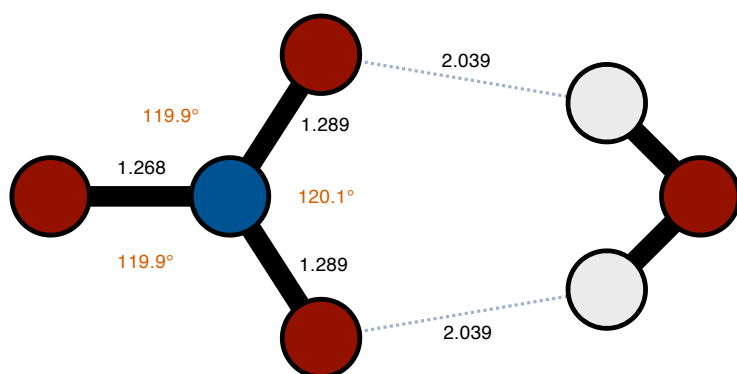


Figure 4.28: Schematic representation of the global minimum geometry ①. This particular geometry is as optimised with MP2/AUG-cc-pVTZ.

Method	6-311G(d,p)	AUG-cc-pVTZ
MP2	44.7615	★ 37.7875
HF	38.5526	29.8887
BLYP	49.0379	34.2659
B3LYP	45.1929	33.7590

Table 4.7: Asymmetric stretch splits by method and basis set in geometry ③.

mations, with B3LYP being close in geometries ① and ③.

The exceptions are the cases of HF and MP2 in geometry ②, which show extreme divergence from the trend. Checking the optimised geometries of these calculations by eye, it is clear that the methods in geometry ② have found very different constrained minima. I will thus not consider the results from this geometry in selecting and calibrating a method.

I ADDED A WATER MOLECULE and optimised the geometry of $[\text{NO}_3 \cdot (\text{H}_2\text{O})_2]^-$ to find the global minimum of this structure, which I'll label geometry ④. Figure 4.32 shows this optimised geometry computed using MP2/AUG-cc-pVTZ. The two water molecules each form H-bonds to two of the nitrate oxygen atoms, with distances between ~ 1.8 and 2.4 \AA . The presence of the water molecules makes each of the NO bonds different lengths, breaking its symmetry to C_s . We see that the NO bond H-bonded to two water molecules is longest, and that the three internal angles are different.

The asymmetric stretch splits at each level of theory for $[\text{NO}_3 \cdot (\text{H}_2\text{O})_2]^-$ geometry ④ are listed in table 4.8, and shown in figure 4.33. We again see that the splitting using the 6-311G(d,p) basis set is larger than that using the AUG-cc-pVTZ, to a greater extent in this geometry, up to 85%. We also see again that the HF method makes lower approximations to the splitting than the reference MP2. In this ge-

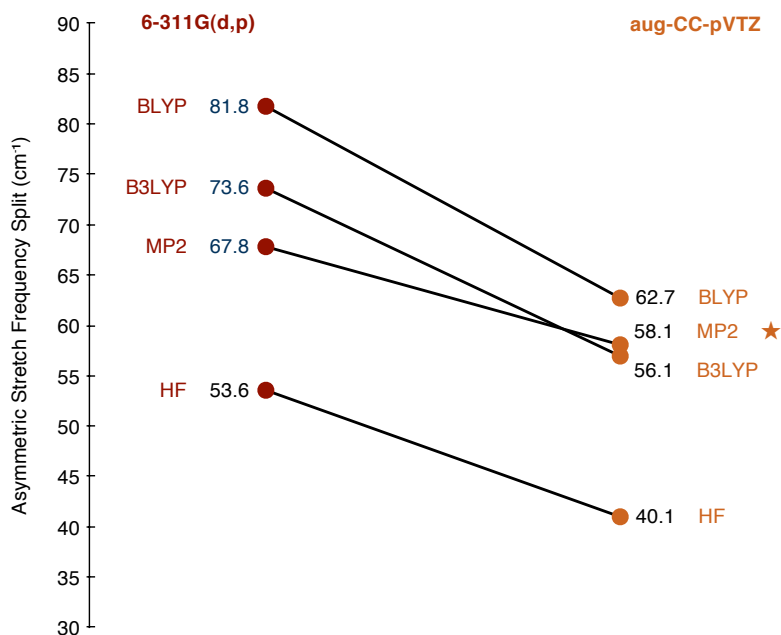


Figure 4.29: Asymmetric stretch splits by method and basis set in geometry ①. The reference MP2/AUG-cc-pVTZ is marked (★).

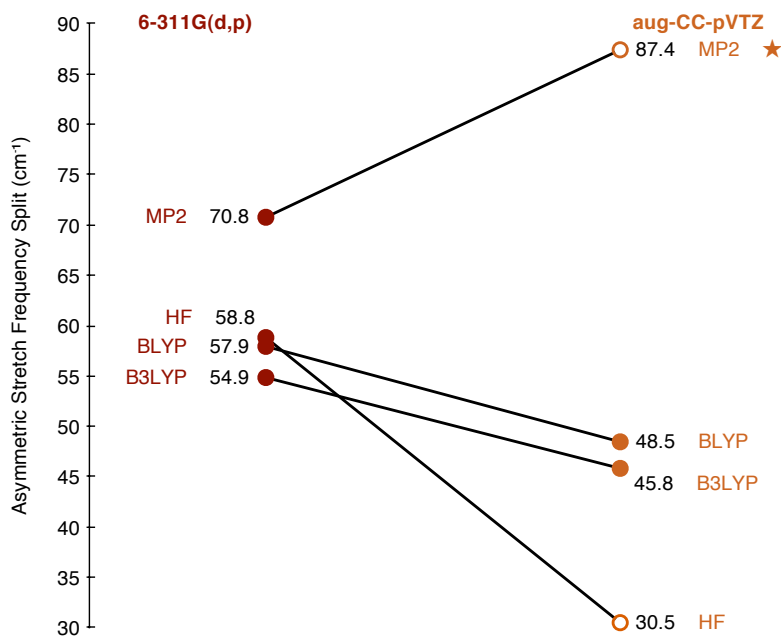


Figure 4.30: Asymmetric stretch splits by method and basis set in geometry ②. We see extreme diversion from the trend using MP2 and HF with the AUG-cc-pVTZ basis set, due to inconsistent optimisation.

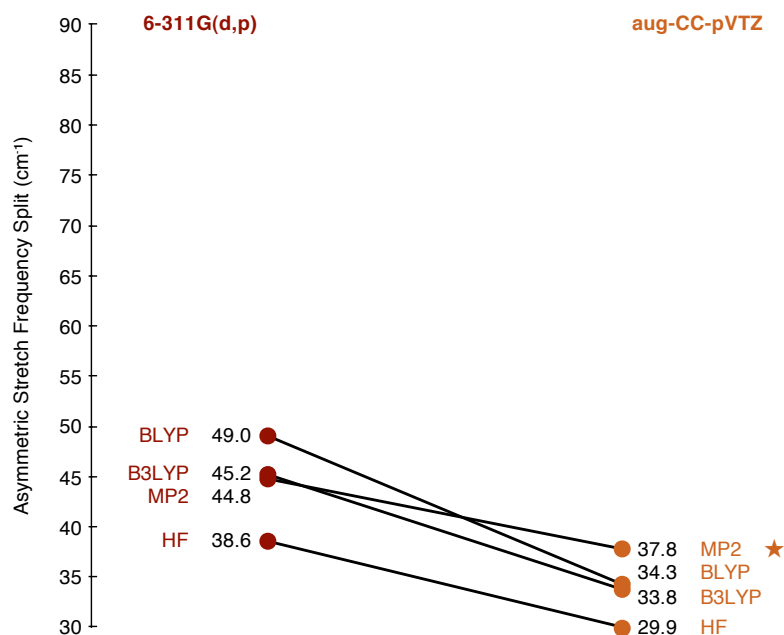


Figure 4.31: Asymmetric stretch splits by method and basis set in geometry ③.

ometry, BLYP and B3LYP make slightly higher approximations than MP2 using the 6-311G(d,p) basis set and slightly lower approximations using AUG-CC-PVTZ.

Method	6-311G(d,p)	AUG-CC-PVTZ
MP2	55.0233	* 34.5218
HF	42.0480	25.9633
BLYP	58.4898	29.6413
B3LYP	55.9699	30.6604

Table 4.8: Asymmetric stretch splits by method and basis set in geometry ④.

Due to the computational expense of using the MP2 method and the AUG-CC-PVTZ basis set, I selected the less-expensive but stable and accurate DFT method B3LYP with the 6-311G(d,p) basis set to continue with calculations on larger complexes in section 4.2.3. To determine the asymmetric split using this combination quantitatively to a level of accuracy close to that of using MP2/AUG-CC-PVTZ, I suggest a calibration factor of 0.75.

4.2.3 Nitrate in a hydration shell

To investigate the symmetry breaking of the asymmetric modes in more realistic solvent environments, I wished to look at larger structures featuring complete hydration shells. As I found in the RDFs from the MD results of section 4.1.1, these shells should feature around 9 to 10 water molecules.

The MD simulations also provide realistic structures within their saved trajectories. Using the cutout script,⁸ I cut out 10 such geometries from an MD simulation at 300 K and 0.1 M, taken every

⁸ see Appendix [??].

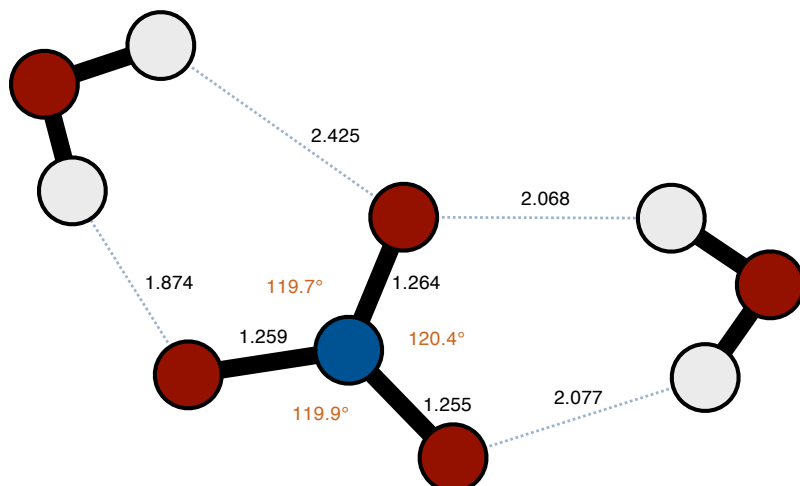


Figure 4.32: Schematic representation of the global minimum geometry ④. This particular geometry is as optimised with MP2/AUG-cc-pVTZ.

50 ps to avoid correlation. I label these geometries ①, ②, ③, ... ⑩.

Geometry ①, which comprises of nitrate surrounded by 8 water molecules, is illustrated in figure 4.34.

I performed geometry optimisation and calculated vibrational modes on these hydration shell complexes, using the B3LYP method and 6-311G(d,p) basis set as selected from the results from the small complexes in section 4.2.2. I fixed the geometry of the water molecules, while the nitrate molecule degrees of freedom remained free.

	ν_{3lo}	ν_{3hi}	$\Delta\nu$	$0.75 \times \Delta\nu$
①	1375.23	1419.75	44.5211	33.39
②	1310.20	1359.03	48.8263	36.62
③	1357.95	1411.92	53.9771	40.48
④	1318.99	1444.56	125.5736	94.18
⑤	1375.30	1453.86	78.5674	58.93
⑥	1392.15	1469.86	77.7143	58.29
⑦	1354.59	1465.72	111.1346	83.35
⑧	1356.62	1480.89	124.2634	93.20
⑨	1373.25	1418.25	45.0098	33.76
⑩	1250.45	1256.64	6.1893	4.64

Table 4.9: Frequencies of the two asymmetric stretch modes calculated for the 10 cutout geometries. Their difference $\Delta\nu$ is the frequency splitting.

With the geometries optimised, I performed a vibrational analysis. The frequencies corresponding to the asymmetric stretches ν_{3lo} and ν_{3hi} are listed in table 4.9. The split between them is listed alongside the same result factored by 0.75 to bring the B3LYP/6-311G(d,p) method and basis set used in line with the reference MP2/AUG-cc-pVTZ level of theory. Though 10 geometries is not enough to make any statistical claims, the results look plausibly in line with the experimental average splits of 60 to 65 cm^{-1} described

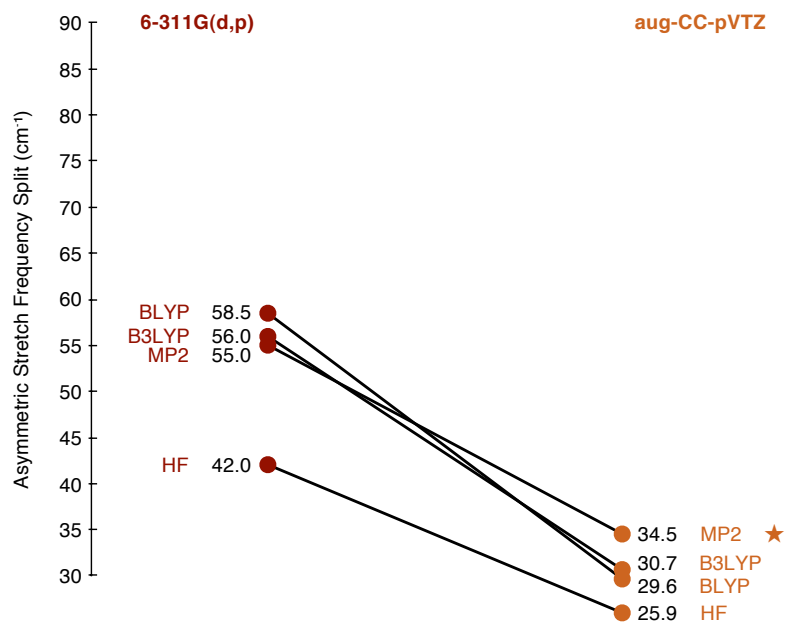


Figure 4.33: Asymmetric stretch splits by method and basis set in geometry ④. The reference MP2/aug-cc-pVTZ is marked (*).

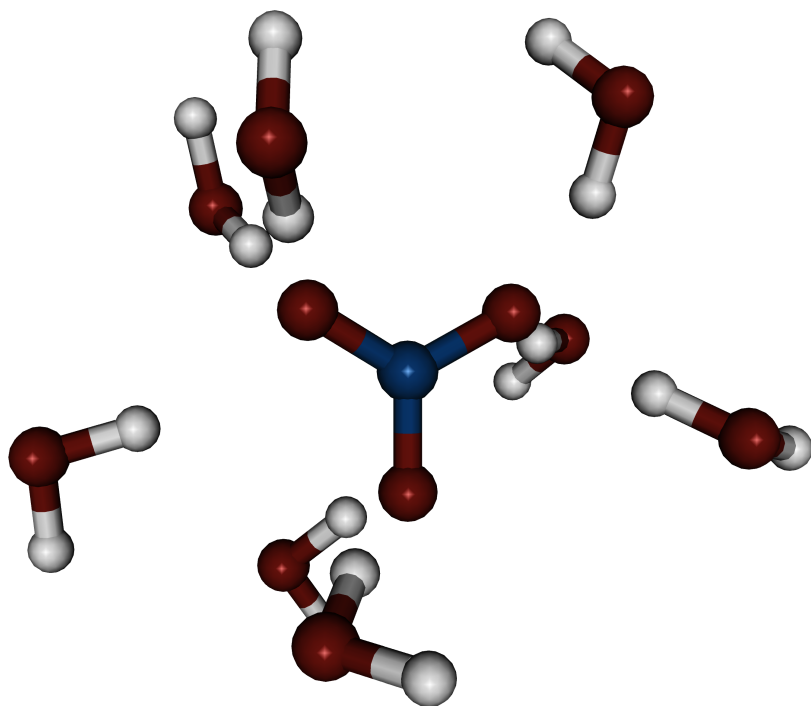


Figure 4.34: An example hydration shell, geometry ⑤, cut out from the MD simulation.

in section 1.1.

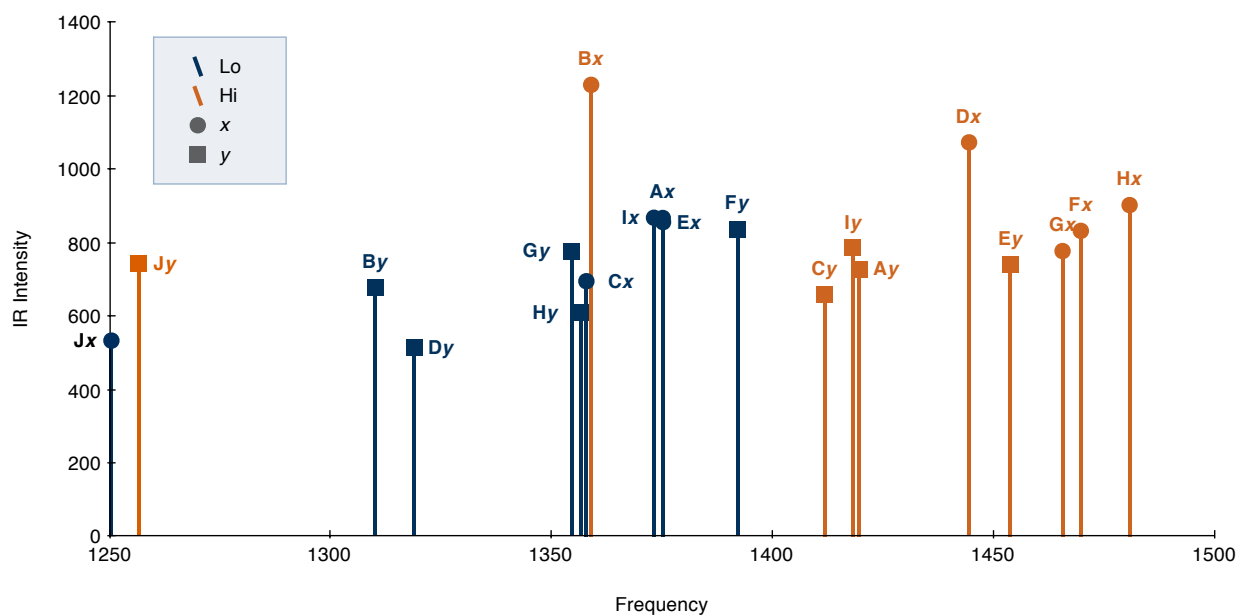


Figure 4.2.3 shows these same frequency peaks plotted together, with colour of each peak indicating whether it is $\nu_{3\text{hi}}$ or $\nu_{3\text{lo}}$ for that particular geometry, and the shape indicating whether it is ν_{3x} or ν_{3y} . We see the peaks perhaps forming into two rough bands, but it is not clear what causes ν_{3x} to be the lower and ν_{3y} the higher frequency, or vice versa.

	N-O ₁		N-O ₂		N-O ₃		$\nu_{3\text{lo}}$
Ⓐ	1.25633	↓	1.25229	↓	1.25229	↑	<i>x</i>
Ⓑ	1.27420	↑	1.27007	↑	1.25666	↓	<i>y</i>
Ⓒ	1.25254	↓	1.25435	↓	1.27021	↑	<i>x</i>
Ⓓ	1.27253	↑	1.26524	↑	1.24293	↓	<i>y</i>
Ⓔ	1.25023	↓	1.24462	↓	1.26877	↑	<i>x</i>
Ⓕ	1.26321	↑	1.25316	↓	1.23759	↓	<i>y</i>
Ⓖ	1.25768	↓	1.27485	↑	1.23667	↓	<i>y</i>
Ⓗ	1.25812	↓	1.27000	↑	1.23495	↓	<i>y</i>
Ⓘ	1.25171	↓	1.25427	↓	1.26392	↑	<i>x</i>
Ⓢ	1.28243	↑	1.29257	↑	1.28107	↑	<i>x</i>

Table 4.10: The optimised length of the internal nitrate bonds between nitrogen and each of the three oxygen atoms for each hydration shell geometry. The arrows (↑ and ↓) indicate whether that bond length has increased or decreased relative to the isolated ion bond length 1.2595 Å. The *x* or *y* in the $\nu_{3\text{lo}}$ column indicates which of the asymmetric stretch modes ν_{3x} or ν_{3y} is lowest in the split.

THE OPTIMISED BOND LENGTHS for each geometry are listed in table 4.10. The arrows (↑ and ↓) indicate whether that bond length has increased or decreased relative to the isolated ion bond length using this method, 1.2595 Å. The *x* or *y* in the $\nu_{3\text{lo}}$ column indicates which of the asymmetric stretch modes ν_{3x} or ν_{3y} is lowest in the split. The clear pattern from these 10 hydration shell geometries suggests that ν_{3x} is $\nu_{3\text{lo}}$ when the N-O₃ bond length is increased. That is, the low frequency corresponds to the strongest H-bonding, be that ν_{3x} or ν_{3y} .

This gives us a link between the internal geometry of the nitrate anion and the ν_{3x} and ν_{3y} vibrations. The length of the N-O bonds are a measure of the H-bonding interaction from the solvent. However, the low frequency vibrational dipole transition moment direction is not always along an N-O bond.

4.2.4 Excited States

To determine which orbitals might be involved in the excitation by the 200 nm UV pulse in the pump-probe experiment,⁹ I calculated excited states for each of the hydration shell structures above using the time-dependent DFT method, which is a linear response method for describing electronically-excited states.

The two most prominent excitations have frequencies of 194.80 nm and 189.08 nm. These excitations, centred on the anion, consist of 'degenerate' π orbitals being excited to the LUMO, a π^* orbital.

The molecular orbitals involved in the 194.80 nm excitation are shown in figure 4.35. The solvent breaks symmetry and mixes π and σ orbitals. The transition dipoles of these excitations lie in the plane of the molecule.

⁹ See section 1.3 for a description of the experiment.

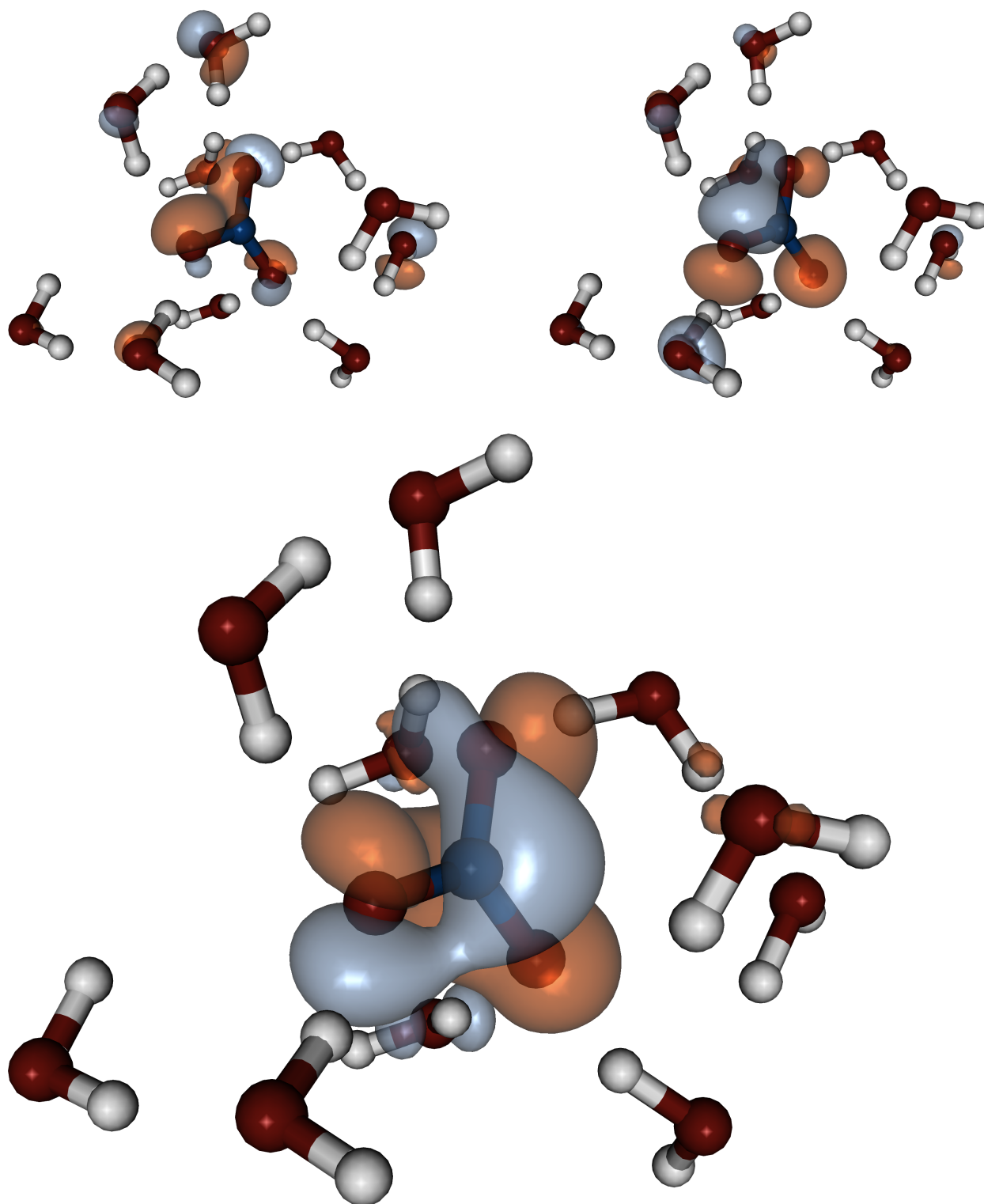


Figure 4.35: The 194.80 nm excitation consists of 'degenerate' π orbitals (top left, top right) being excited to the LUMO (bottom).

5

Conclusions

We see two distinct reorientation rates in the second-rank TCFs of the MD simulations, one ultrafast (sub-picosecond), which I attribute to librational motion of the nitrate anion, and one slower (picosecond), which I attribute to large angular jumps by the anion due to transient hydration shell structure.

The time constants of both reorientation mechanisms decrease linearly with increased temperature.

I determine the activation energy of the H-bond-breaking mechanism to be $\sim 13 \text{ kJ} \cdot \text{mol}^{-1}$, comparable to the H-bond energy of ~ 16 to $20 \text{ kJ} \cdot \text{mol}^{-1}$.

THE EXPERIMENTAL RESULTS by Thøgersen et al.¹ show a clear frequency dependence in the anisotropy decay of pump-probe spectroscopy of nitrate in solution. In the reorientation TCF results of my MD simulations² I only find clear anisotropy at the lowest temperature, 280 K, and that is a slower rotation in the vector normal to the nitrate plane with no distinction between the perpendicular in-plane vectors.

The problem is that the x and y vectors of the symmetry-broken vibrational frame *depend* on the transient interactions of the solvent and fluctuate accordingly. The directions of i and j are fixed in the trajectory analysis and so mix x and y together, losing any information about frequency dependence.³

FROM THE PATTERN in the hydration shell vibrational analysis, we now have a link between the geometry of the anion — in particular the length of the N-O₃ bond — and the symmetry-breaking interaction from the solvent. Although a useful clue, this does not allow me to analyse the MD trajectory directly, as these bond lengths have been post-optimised by the QC calculation.

The next step required is to determine the link between the length of the N-O bonds and the hydration structure, for example via the number of H-bonds, their distances and angles. This knowledge would allow me to manipulate the MD trajectory files before analysis, such that i is set to be x and j to be y through the simulation. I could then analyse these vectors with a second-rank reorientation TCF, as before. I believe that if the solvation is flexible

¹ As described in section 1.3.

² See section 4.1.2.

³ Compare figures 1.2 and 1.3 with figure 4.16 for descriptions of x , y and i , j .

enough, the TCF would show the frequency-dependence.

However, it is important to note that such a TCF would not be a physical reorientation following a molecular vector, as the i and j would fluctuate with the symmetry-breaking. It is what we might call a 'pseudo-reorientation' of the low frequency dipole transition moment.

THE THEORETICAL RESULTS presented in this thesis throw light on the reorientation dynamics of nitrate in water, but are insufficient to explain the frequency-dependence observed in the Aarhus experiments in terms of this reorientation. Firstly, I believe that the classical MD simulations do not accurately describe the cooperative nature of H-bonding. Secondly, I have not directly modelled the reorientation of the vibrational transition dipole moment. Along with solving these problems, an investigation should be made into any relation between the asymmetric stretch transitions and the CTS transitions.

I hope this work will help in the final description of what is a compelling experimental result.

A

The Cutout Tool

During this study I required various small tools to manipulate trajectories, in particular to cut hydration shell geometries from MD trajectories for use in QC calculations.

To enable this, I built an object-oriented C++ framework for handling atoms, molecules and ensembles with the ability to read and write geometry and trajectory files in cartesian format (XYZ). The intention is that this framework can be used to quickly write arbitrary tools for working with molecules on further work.

THE CUTOUT TOOL takes a Cartesian format (XYZ) molecular trajectory file and cuts out whole molecules in a given range of a any position, returning a new XYZ file. It calculates intermolecular bonds based on user-defined parameters.

The code, along with the framework, is open source and available to download or fork at <http://github.com/tommyogden/cutout>.

Acknowledgements

I thank Michael Odelius for teaching me the tools of molecular dynamics and quantum chemistry, for bringing me this problem to study and for all the time and knowledge he has shared in helping me complete this work.

I thank Søren Keiding and Jan Thøgersen for trusting me with this interesting problem and for their generous hospitality in welcoming me to Aarhus.

I thank Ida Josefsson for helping me understand many physical concepts and for sharing her experience in the tricks of the quantum chemist's trade.

I thank Nils Elander for his kind and valuable advice.

I thank the Molecular Physics department at Stockholm University for their friendliness and for our enjoyable conversations over afternoon fika.

Bibliography

J.P.D Abbatt. Interaction of HNO_3 with water-ice surfaces at temperatures of the free troposphere. *Geophysical Research Letters*, 24(12):1479–1482, 1997.

M. P. Allen and D. J. Tildesley. *Computer Simulation of Liquids*. Clarendon Press, first edition, June 1989.

K Capelle. A bird's-eye view of density-functional theory. *Brazilian Journal of Physics*, 36:1318–1343, 2006.

P Debye. Polar molecules. *Chemical Catalog Co.*, 1929.

M. J. Frisch, G. W. Trucks, H. B. Schlegel, G. E. Scuseria, M. A. Robb, J. R. Cheeseman, J. A. Montgomery, Jr., T. Vreven, K. N. Kudin, J. C. Burant, J. M. Millam, S. S. Iyengar, J. Tomasi, V. Barone, B. Mennucci, M. Cossi, G. Scalmani, N. Rega, G. A. Petersson, H. Nakatsuji, M. Hada, M. Ehara, K. Toyota, R. Fukuda, J. Hasegawa, M. Ishida, T. Nakajima, Y. Honda, O. Kitao, H. Nakai, M. Klene, X. Li, J. E. Knox, H. P. Hratchian, J. B. Cross, V. Bakken, C. Adamo, J. Jaramillo, R. Gomperts, R. E. Stratmann, O. Yazyev, A. J. Austin, R. Cammi, C. Pomelli, J. W. Ochterski, P. Y. Ayala, K. Morokuma, G. A. Voth, P. Salvador, J. J. Dannenberg, V. G. Zakrzewski, S. Dapprich, A. D. Daniels, M. C. Strain, O. Farkas, D. K. Malick, A. D. Rabuck, K. Raghavachari, J. B. Foresman, J. V. Ortiz, Q. Cui, A. G. Baboul, S. Clifford, J. Cioslowski, B. B. Stefanov, G. Liu, A. Liashenko, P. Piskorz, I. Komaromi, R. L. Martin, D. J. Fox, T. Keith, M. A. Al-Laham, C. Y. Peng, A. Nanayakkara, M. Challacombe, P. M. W. Gill, B. Johnson, W. Chen, M. W. Wong, C. Gonzalez, and J. A. Pople. Gaussian 03, revision c.02, 2004. Gaussian, Inc., Wallingford, CT.

David J. Griffiths. *Introduction to Quantum Mechanics*. Pearson Education, second edition, May 2003.

C Guimbaud, F Arens, L Gutzwiller, HW Gäggeler, and M Ammann. Uptake of HNO_3 to deliquescent sea-salt particles. *Atmospheric Chemistry and Physics*, 2(4):249–257, 2002.

S Jayaraman, AP Thompson, OA von Lilienfeld, and EJ Maginn. Molecular simulation of the thermal and transport properties of three alkali nitrate salts. *Ind. Eng. Chem. Res.*, 49(2):559–571, 2010.

- Frank Jensen. *Introduction to Computational Chemistry*. Wiley-Blackwell, second edition, October 2006.
- D Laage. A molecular jump mechanism of water reorientation. *Science*, 311(5762):832–835, Feb 2006.
- D Laage and J.T Hynes. Reorientational dynamics of water molecules in anionic hydration shells. *Proceedings of the National Academy of Sciences*, 104(27):11167, 2007.
- Damien Laage, Guillaume Stirnemann, Fabio Sterpone, Rossend Rey, and James T Hynes. Reorientation and allied dynamics in water and aqueous solutions. *Annu. Rev. Phys. Chem.*, 62(1):395–416, May 2011.
- A Laaksonen and H Kovacs. Silver nitrate in aqueous solution and as molten salt: A molecular dynamics simulation and nmr relaxation study. *Canadian Journal of Chemistry*, 72(11):2278–2285, 1994.
- MCG Lebrero, DE Bikiel, MD Elola, DA Estrin, and AE Roitberg. Solvent-induced symmetry breaking of nitrate ion in aqueous clusters: A quantum-classical simulation study. *The Journal of Chemical Physics*, 117:2718, 2002.
- E W Lemmon, M O McLinden, and D G Friend. *Thermophysical Properties of Fluid Systems in NIST Chemistry WebBook, NIST Standard Reference Database Number 69*, Eds. P.J. Linstrom and W.G. Mallard. National Institute of Standards and Technology, Gaithersburg MD, 2011.
- A.P Lyubartsev and A Laaksonen. M. dynamix — a scalable portable parallel MD simulation package for arbitrary molecular mixtures. *Computer physics communications*, 128(3):565–589, 2000.
- D Madsen, J Larsen, S.K Jensen, S.R Keiding, and J Thøgersen. The primary photodynamics of aqueous nitrate: Formation of peroxyxynitrite. *Journal of the American Chemical Society*, 125(50):15571–15576, 2003.
- Masaru Nakahara and Keiji Emi. Effect of dielectric friction on the perpendicular reorientation of the nitrate ion in water and organic solvents. *The Journal of Chemical Physics*, pages 1–8, Jul 1999.
- Lavanya M. Ramaniah, Marco Bernasconi, and Michele Parrinello. Ab initio molecular-dynamics simulation of k^+ solvation in water. *The Journal of Chemical Physics*, 111(4):1587–1591, 1999.
- S.G Ramesh, S Re, J Boisson, and J.T Hynes. Vibrational symmetry breaking of NO_3^- in aqueous solution: NO asymmetric stretch frequency distribution and mean splitting. *The Journal of Physical Chemistry A*, 114(3):1255–1269, 2009.

V.H Smith, G.D Tilman, and J.C Nekola. Eutrophication: impacts of excess nutrient inputs on freshwater, marine, and terrestrial ecosystems. *Environmental pollution*, 100(1-3):179–196, 1999.

Kazuko Tanaka. Self-diffusion coefficients of water in pure water and in aqueous solutions of several electrolytes with ^{18}O and ^2H as tracers. *Journal of the Chemical Society, Faraday Transactions 1*, 74: 1879–1881, 1978.

Jos Thijssen. *Computational Physics*. Cambridge University Press, second edition, March 2007.

Jan Thøgersen. Rotational anisotropy of aqueous nitrate. *Unpublished note*, Jul 2011.

Jan Thøgersen, Svend Knak Jensen, Christian Petersen, and Søren R Keiding. Reorientation of hydroxide ions in water. *Chemical Physics Letters*, 466(1-3):1–5, Mar 2008.

V Vchirawongkwin, H Sato, and S Sakaki. Rism-scf-sedd study on the symmetry breaking of carbonate and nitrate anions in aqueous solution. *The Journal of Physical Chemistry B*, 2010.

M.R Waterland and A.M Kelley. Far-ultraviolet resonance raman spectroscopy of nitrate ion in solution. *The Journal of Chemical Physics*, 113:6760, 2000.

M.R Waterland, D Stockwell, and A.M Kelley. Symmetry breaking effects in no: Raman spectra of nitrate salts and ab initio resonance raman spectra of nitrate–water complexes. *The Journal of Chemical Physics*, 114:6249, 2001.

M Whittle and JHR Clarke. Nitrate ion reorientation in aqueous calcium nitrate solutions: new evidence for ion association. *Chemical Physics Letters*, 98(2):172–175, 1983.

World Health Organisation. *Guidelines for Drinking-water Quality*. WHO Press, third edition, 2008.